

A Comprehensive Analysis of *Fermi* Gamma-Ray Burst Data. I. Spectral Components and Their Possible Physical Origins of LAT/GBM GRBs

Bin-Bin Zhang¹, Bing Zhang¹, En-Wei Liang^{1,2}, Yi-Zhong Fan^{3,1}, Xue-Feng Wu^{1,3}, Asaf Pe'er⁴,
Amanda Maxham¹, He Gao¹, Yun-Ming Dong^{1,5}

ABSTRACT

We present a systematic analysis of the spectral and temporal properties of 17 gamma-ray bursts (GRBs) co-detected by Gamma-Ray Monitor (GBM) and Large Area Telescope (LAT) on board the *Fermi* satellite by May 2010. We performed a time-resolved spectral analysis of all the bursts with the finest temporal resolution allowed by statistics, in order to reduce temporal smearing of different spectral components. We found that the time-resolved spectra of 14 out of 17 GRBs are best modeled with the classical “Band” function over the entire *Fermi* spectral range, which may suggest a common origin for emissions detected by LAT and GBM. GRB 090902B and GRB 090510 require the superposition of a MeV component and an extra power law component, with the former having a sharp cutoff above E_p . For GRB 090902B, this MeV component becomes progressively narrower as the time bin gets smaller, and can be fit with a Planck function as the time bin becomes small enough. In general, we speculate that phenomenologically there may be three elemental spectral components that shape the time-resolved GRB spectra: a Band-function component (e.g. in GRB 080916C) that extends in a wide energy range and does not narrow with decreasing time bins, which may be of non-thermal origin; a quasi-thermal component (e.g. in GRB 090902B) with the spectra progressively narrowing with reducing time bins; and another non-thermal power law component extending to high energies. The spectra of different bursts may be decomposed into one or more of these elemental components. We compare this sample with the BATSE sample and investigate some correlations among spectral parameters. We discuss the physical implications of the data analysis results for GRB prompt emission, including jet composition (matter-dominated vs. Poynting-flux-dominated outflow), emission sites (internal shock, external shock or photosphere),

¹Department of Physics and Astronomy, University of Nevada Las Vegas, Las Vegas, NV 89154, USA.

²Department of Physics, Guangxi University, Guangxi 530004, China.

³Purple Mountain Observatory, Chinese Academy of Sciences, Nanjing 210008, China

⁴Space Telescope Science Institute, 3700 San Martin Drive, Baltimore, MD 21218, USA ; Riccardo Giacconi fellow

⁵Department of Physics, Sichuan Normal University, Sichuan 530004, China.

as well as radiation mechanisms (synchrotron, synchrotron self-Compton, or thermal Compton upscattering).

Subject headings: gamma-ray burst: general

1. Introduction

Although observationally accessed much earlier, GRB prompt emission is still less understood than afterglow. The fundamental uncertainties lie in the following three poorly known important properties of GRBs (e.g. Zhang & Mészáros 2004 for a review): (1) Ejecta composition: Are the ejecta mostly composed of baryonic matter or a Poynting flux? (2) Energy dissipation site: Is the emission from internal shocks (Rees & Mészáros 1994; Kobayashi et al. 1997), the photosphere (Paczýnski 1986; Goodman 1986; Mészáros & Rees 2000; Mészáros et al. 2002; Pe’er 2008), some magnetic dissipation regions (Lyutikov & Blandford 2003; Zhang & Yan 2011), or the external shock (Rees & Mészáros 1992; Mészáros & Rees 1993; Dermer & Mitman 1999)? (3) Is the radiation mechanism synchrotron/jitter radiation (Mészáros et al. 1994; Medvedev 2000), synchrotron self-Compton (Panaitescu & Mészáros 2000; Kumar & McMahon 2008), or Comptonization of thermal photons (e.g. Thompson 1994; Pe’er et al. 2005, 2006; Beloborodov 2010; Lazzati & Begelman 2009)?

Before *Fermi*, understanding of GRB prompt emission has progressed slowly. Observations of early X-ray afterglows by *Swift* revealed a steep decay phase that is smoothly connected to prompt emission (Tagliaferri et al. 2005; Barthelmy et al. 2005), which suggests that the prompt emission region is detached from the afterglow emission region, and that the prompt emission site is “internal” (Zhang et al. 2006). Other than this, the properties of prompt emission were poorly constrained. The main factor that hampers progress has been the narrow energy band of the gamma-ray detectors of previous missions. Theoretical models usually predict rich features in the prompt spectra (e.g. Pe’er et al. 2006, see Zhang 2007; Fan & Piran 2008 for reviews on high energy emission processes). However, within the narrow observational spectral window, these features cannot be fully displayed. Instead, most previous spectral analyses revealed an empirical “Band”-function (Band et al. 1993), which is a smoothly-joint broken power law, whose physical origin is not identified. For the bright BATSE GRB sample, the typical low and high energy photon indices are distributed around $\alpha \sim -1$ and $\beta \sim -2.2$, respectively, while the spectral peak energy E_p is distributed around 200-300 keV (Preece et al. 2000). Later observations suggested that the distribution of E_p can be much wider, extending to a few keV in the soft regime for X-ray flashes (Sakamoto et al. 2005) and to greater than 100 MeV in the hard regime (e.g. $\gtrsim 170$ MeV for GRB 930506, Kaneko et al. 2008). Some BATSE GRBs were also detected by EGRET in the GeV range (Kaneko et al. 2008). For example, It was found that the GeV emission can last much longer than the MeV emission (e.g. GRB 940217, Hurley et al. 1994), and that it can form a distinct spectral component (e.g. GRB 941017, González et al. 2003). In the softer regime, an X-ray excess

component with respect to the Band function was discovered in some BATSE GRBs (Preece et al. 1996). However, the previous data were not adequate to place meaningful constraints on the three main questions discussed above.

The *Fermi* satellite ushered in a new era of studying GRB prompt emission. The two instruments on board *Fermi*, the Gamma-ray Burst Monitor (GBM; Meegan et al. 2009) and the Large Area Telescope (LAT; Atwood et al. 2009), provide an unprecedented spectral coverage for 7 orders of magnitude in energy (from ~ 8 keV to ~ 300 GeV). Since the beginning of GBM/LAT science operation in August 2008 and as of the writing of this paper (May 2010), there have been 17 GRBs co-detected by LAT and GBM, with a detection rate comparable to the expectation assuming that the LAT-band emission is the simple extrapolation of the Band spectrum to the GeV range (Abdo et al. 2008; Lü et al. 2010). As will be shown below, the Band-function fits apply to most LAT GRBs, although some outliers do exist. Broad band spectral analyses have been published by the *Fermi* team for several individual GRBs, e.g. GRB 080916C (Abdo et al. 2009a), GRB 090510 (Abdo et al. 2009b, Ackermann et al. 2010), GRB 090902B (Abdo et al. 2009c, Ryde et al. 2010), GRB 080825C (Abdo et al. 2009d), and GRB 081024B (Abdo et al. 2010a), which revealed several interesting features, such as the nearly featureless Band spectra covering 6 orders of magnitude in all epochs for GRB 080916C, the existence of an extra power law component extending to high energies in GRB 090510 and GRB 090902B, the existence of a quasi-thermal emission component in GRB 090902B, the delayed onset of the LAT-band emission with respect to the GBM-band emission, as well as an extended rapidly decaying GeV afterglow for most GRBs.

These discoveries have triggered a burst of theoretical investigations of GRB prompt emission. Zhang & Pe’er (2009) argued that the lack of a thermal component in the nearly featureless spectra of GRB 080916C suggests a Poynting flux dominated flow for this burst. The conclusion was strengthened by a follow up study of Fan (2010, see also Gao et al. 2009). On the other hand, the quasi-thermal component in GRB 090902B (Ryde et al. 2010) is well-consistent with the photosphere emission of a hot fireball (Pe’er et al. 2010, Mizuta et al. 2010), suggesting that the burst is not highly magnetized. The possibility that the entire Band function spectrum is photosphere emission was discussed by several authors (Fan 2009; Toma et al. 2010; Beloborodov 2010; Lazzati & Begelman 2010; Ioka 2010). These models have specific predictions that can be tested by the available data. In the high energy regime, Kumar & Barniol Duran (2009, 2010), Ghisellini et al. (2010) and Wang et al. (2010) suggested that the GeV afterglow is of external shock origin, which requires some unconventional parameters (Li 2010a; Piran & Nakar 2010). On the other hand, the fact that LAT emission is the natural spectral extension of GBM emission in some GRBs suggests that the GeV emission may be of an internal origin similar to MeV emission (Zhang & Pe’er 2009). Finally, the delayed onset of the GeV emission has been interpreted as emergence of the upscattered cocoon emission (Toma et al. 2009), synchrotron emission from shock accelerated protons (Razzaque et al. 2009), as well as delayed residual internal shock emission (Li 2010b). Again these models have specific predictions that may be tested by a detailed analysis of the data.

Our goal is to systematically analyze the GRB data collected by the *Fermi* mission, aiming

at addressing some of the above mentioned problems in prompt GRB emission physics. Here we report the first paper in the series, which focuses on a comprehensive analysis of the GRBs that were co-detected by LAT and GBM. This sample has a much broader spectral coverage than the GBM-only GRBs, and therefore carries much more information about GRB prompt emission. The plan of the paper is the following. In Section 2 we describe the details of our sample selection and data analysis method. The data analysis results are presented in Section 3, with emphases on the unique features of some GRBs. We also present spectral parameter distributions and some possible correlations. In Section 4, we summarize the results and speculate on the existence of at least three elemental spectral components, and discuss their possible physical origins and possible combinations. In Section 5, we present the comparison between the emissions detected in the GBM band and that detected in the LAT band and discuss their physical connections. Our conclusions are summarized in Section 6 with some discussion.

2. Sample and Data Reduction

As of May 2010, 17 GRBs have been co-detected by *Fermi* LAT and GBM. Our sample includes all 17 GRBs (Table 1). We downloaded the GBM and LAT data for these GRBs from the public science support center at the official *Fermi* web site <http://fermi.gsfc.nasa.gov/ssc/data/>. An IDL code was developed to extract the energy-dependent lightcurves and time-dependent spectra for each GRB. This code was based on the *Fermi* RMFIT package (V3.3), the *Fermi* Science Tools (v9r15p2) and the HEASOFT tools, which allows a computer to extract lightcurves and spectra automatically. The human involvement is introduced later to refine the analysis when needed. The code automatically performs the following tasks.

1. Extract the background spectrum and lightcurve of the GBM data. *Fermi* records GBM data in several formats. For background reduction we use the CSPEC format data because it has a wider temporal coverage than the event data (time-tagged event, TTE, format). The background spectrum and lightcurve are extracted from some appropriate time intervals before and after the burst¹, and the energy-dependent background lightcurves are modeled with a polynomial function $B(E_{\text{ch}}, t)$, where E_{ch} is a specified energy band.
2. Extract the source spectrum and lightcurve of the GBM data. This is done with the event (TTE) data. GBM has 12 NaI detectors (8 keV–1 MeV) and 2 BGO detectors (200 keV–40 MeV). The overall signal-to-noise ratio (SNR) and peak count rate are calculated for each detector. The brightest NaI and BGO detectors are usually used for the analyses. If several

¹ An appropriate background time interval is typically when the lightcurve is “flat” with Poisson noise photons. For each burst, we select background time intervals as $[-t_{b,1}, -t_{b,1}]$ before the burst and $[t_{b,3}, t_{b,4}]$ after the burst, where t_b ’s are typically in the order of tens to hundreds of seconds. The exact values vary for different bursts due to their different brightnesses and the corresponding orbit slewing phases.

detectors have comparable brightnesses, all of them (usually 2-4 detectors) are taken for the analyses. By subtracting the background spectrum and lightcurve obtained in the previous step, the time-dependent spectra and energy-dependent lightcurves of the source in the GBM band are then obtained.

3. Estimate the LAT-band background. Since only a small number of photons are detected by LAT for most GRBs, the background estimation should be performed cautiously. It is not straightforward to estimate an accurate LAT background using off-source regions around the trigger time. In our analyses, the LAT background is extracted using on-source region data long after the GBM trigger when the photon counts merge into a Poisson noise.
4. Extract the LAT-band spectrum and lightcurve. Both “diffuse” and “transient” photons (level 0-3) are included. Since the LAT point spread function (PSF) strongly depends on the incident energy and the convention point of the tracker (Ohno et al. 2010), the photons are grouped into FRONT and BACK classes and their spectra are extracted separately based on different detector response files. The region of interest (ROI) that contains significant counts of LAT photons is further refined when necessary (Atwood et al. 2009; Abdo et al. 2009d).
5. Extract the background-subtracted GBM and LAT lightcurves for different energy bands. In our analysis, the lightcurves are extracted in the following energy bands: 8–150 keV, 150–300 keV, 300 keV–MeV, 1–30 MeV, and the LAT band (above 100 MeV).
6. Make dynamically time-dependent spectral fits. Initially, the burst duration is divided in an arbitrary number of slices. The code then automatically refines the number of slices and the time interval for each slice, so that the photon counts in each bin (typically minimum 20 counts for GBM spectra) give adequate statistics for spectral fitting (the reduced χ^2 is typically in the range of 0.75 - 1.5, a special case is GRB 090510, see Sect.3.2). The time slices are defined to be as small as possible as long as the extracted spectra satisfy these statistical criteria. The GBM spectra of the selected NaI and BGO detectors and the LAT “FRONT” and “BACK” type spectra are all extracted for each slice. These spectra, together with the corresponding response files (using the same one as the CSPEC data for LAT, or generated using gtrsp for GBM) are input into XSPEC (V 12.5.1) simultaneously to perform spectral fitting. The following spectral functions are considered (in order of increasing free parameters): single power law (PL), blackbody (BB, Planck function), power-law with exponential cutoff (CPL), and Band function. The models are tested based on the following principles: (1) If a one-component model can adequately describe the data (giving reasonable reduced χ^2 , say, between 0.75 and 1.5), two-component models are not considered; (2) for one-component models, if a function with less free parameters can describe the data adequately, it is favored over the models with more parameters. (3) In addition, the Akaike’s Information Criterion² (AIC, Akaike 1974) is calculated to evaluate each model by considering both the

²AIC is defined by $AIC = n \ln \left(\frac{\chi^2}{n} \right) + 2k$, where n is the number of data points, k is the number of free parameters

fitting goodness (χ^2) and the complexity of the model. We confirmed that the model with minimal AIC is the preferred model we choose based on the first two criteria. Nonetheless, since most GRBs have a Band-function spectra (see below), we also apply the Band function to those time bins that do not demand it in order to compare the fitting results between the Band function and other functions with less parameters (e.g. power law, blackbody, or power law with exponential cutoff).

To assess the quality of a spectral fit, we use the traditional χ^2 statistics. Due to the low count rate of LAT photons, we use the Gehrels (1986) weighting method in the high energy regime. We also employed the C-stat method (as used by the *Fermi* team), and found that the two methods usually give consistent results. We chose the χ^2 method since it gives more reliable error estimates. All the model fitting parameters and χ^2 statistics are presented in Table 2. For each burst, we present the time-dependent spectral parameters in the designated time bins defined by the statistics of spectral fitting, as well as the time-integrated spectral fit during the entire burst in the last row.

3. Data Analysis Results

The data analysis results are presented in Figs. 1-17. Each figure corresponds to one burst, and contains 10-11 panels. In the left panels, the lightcurves in 5 energy bands (8–150 keV, 150–300 keV, 300 keV–1 MeV, 1–30 MeV, and > 100 MeV) are presented in linear scale, together with the temporal evolution of the spectral parameters (α , β , E_p for Band function, kT for blackbody function, and Γ for single power law photon index). The top right panel is an example photon spectrum with model fitting, typically taken at the brightest time bin. The time-dependent model spectra are presented in the mid-right panel. The time-slices for the time-resolved spectral fitting are marked with vertical lines in the left panel lightcurves. In the bottom right panel, the GBM and LAT lightcurves are presented and compared in logarithmic scale.

In the following, we discuss the results of several individual bright GRBs (Sect.3.1-3.4), and then discuss other GRBs in general (Sect.3.5). We then present statistics of spectral parameters (Sect.3.6) and some possible correlations (Sect.3.7).

3.1. GRB 080916C

As shown in Fig.2, GRB 080916C is a long GRB with a duration ~ 66 s. The entire lightcurve can be divided into 6 segments. The smallest time bins during the brightest epochs (first two) are 3.7 s and 5.4 s, respectively. This corresponds to a rest-frame time interval ≤ 1 s (given its redshift 4.35, Greiner et al. 2009). In all the time intervals, we found that the Band-function gives excellent

of a particular model, and χ^2 is the residual sum of squares from the estimated model (e.g. Shirasaki et al. 2008).

fits to the data, consistent with Abdo et al. (2009a). Initially there is a spectral evolution where the spectra “widen” with time (α hardening and β softening), but later the spectral parameters essentially do not evolve any more. We note that the steep β in the first time bin is mostly because of the non-detection in the LAT band. The tight upper limit above 100 MeV constrains the range of β not to be too hard. On the other hand, with GBM data alone, the data of in first time bin can be still fit as a Band function, with $\beta \sim -2.12^{+0.158}_{-0.107}$ similar to the values at later epochs. This suggests an alternative interpretation to the data: The high energy spectral index may be similar throughout the burst. The delayed onset of LAT-band emission may be because initially there is a spectral cutoff around 100 MeV, which later moves to much higher energies (e.g. above 13.2 GeV in the second time bin).

It is interesting to note that the time integrated spectrum of GRB 080916C throughout the burst is also well fit with a Band function, where the spectral indices do not vary with time resolution. As an example, we present in Fig.18 the νF_ν spectra of GRB 080916C for three time bins with varying time resolution. Remarkably, the parameters do not vary significantly: $\alpha \sim -1.12$, $\beta \sim -2.25$ for 3.5-8 s; $\alpha \sim -1.0$, $\beta \sim -2.29$ for 2-10 s; $\alpha \sim -1.0$, $\beta \sim -2.27$ for 0-20 s. This is in stark contrast with GRB 090902B discussed below.

3.2. GRB 090510

The short GRB 090510 was triggered with a precursor 0.5 s prior to the main burst. Two LAT photons were detected before the main burst. During the first time slice (0.45-0.5 s), no LAT band emission is detected, and the GBM spectrum can be well fit with a PL with an exponential cutoff (CPL hereafter). In the subsequent time slices, an additional PL component shows up, and the time-resolved spectra are best fit by the CPL + PL model. If one uses a Band + PL model to fit the data, the high energy spectral index β of the Band component cannot be constrained. If one fixes β to a particular value, it must be steeper than -3.5 in order to be consistent with the data. The CPL invoked in these fits has a low energy photon index $\Gamma_{\text{CPL}} \sim -(0.6 - 0.8)$, which is very different from the case of a BB (where $\Gamma_{\text{CPL}} \sim +1$). On the other hand, the high-energy regime (exponential cutoff) is very similar to the behavior of a BB.

Since this is a short GRB, we do not have enough photons to perform very detailed time-resolved spectral analysis. However, in order to investigate spectral evolution and the interplay between the MeV component and the extra PL component, we nonetheless make 4 time bins (see also Ackermann et al. 2010). As a result, the reduced χ^2 of each segment is outside the range of $0.75 \leq \chi^2/\text{dof} \leq 1.5$ as is required for other GRBs. Our reduction results are generally consistent with those of the Fermi team (Abdo et al. 2009b; Ackermann et al. 2010).

3.3. GRB 090902B

The spectrum of GRB 090902B is peculiar. Abdo et al. (2009c) reported that both the time-integrated and time-resolved spectra of this GRB can be fit with the Band+PL model. Ryde et al. (2010) found that the time-resolved spectra can be fit with a PL plus a multi-color blackbody model. This raises the interesting possibility that a blackbody-like emission component is a fundamental emission unit shaping the observed GRB spectra.

In order to test this possibility, we carried out a series of time-resolved spectral analysis on the data (Fig.18). We first fit the time-integrated data within the time interval 0-20 s, and found that it can be fit with a model invoking a Band function and a power law, but with a poor $\chi^2/\text{dof} \sim 3.52$. Compared with the Band component of other GRBs, this Band component is very narrow, with $\alpha \sim -0.58$, $\beta \sim -3.32$. A CPL + PL model can give comparable fit, with $\Gamma_{\text{CPL}} \sim -0.59$. Next we zoom into the time interval 8.5 - 11.5 s, and perform spectral fits. The Band+PL and CPL+PL models can now both give acceptable fits, with parameters suggesting a narrower spectrum. For the Band+PL model, one has $\alpha \sim -0.07$, $\beta \sim -3.69$ with $\chi^2/\text{dof} = 1.26$. For the CPL+PL model, one has $\Gamma_{\text{CPL}} \sim -0.08$ with $\chi^2/\text{dof} = 1.30$. Finally we room in the smallest time bin (9.5 - 10 s) in which the photon counts are just enough to perform adequate spectral fits. We find that the Band + PL model can no longer constrain β . The spectrum becomes even narrower, with $\alpha \sim 0.07$ and $\beta < -5$. The CPL+PL model can fit the data with a range of allowed Γ_{CPL} . In particular, if one fixes $\Gamma_{\text{CPL}} \sim +1$ (the Rayleigh-Jeans slope of a blackbody), one gets a reasonable fit with $\chi^2/\text{dof} = 0.92$. This encourages us to suspect that a blackbody (BB) + PL model can also fit the data. We test it and indeed found that the model can fit the data with $\chi^2/\text{dof} = 1.11$. These different models require different Γ_{PL} for the extra PL component, but given the low photon count rate at high energies, all these models are statistically allowed. Since the BB + PL model has less parameters than the CPL + PL and Band + PL models, we take this model as the simplest model for this smallest time interval.

Next, we tried to divide the lightcurve of GRB 090902B into as many as time bins as possible so that the photon numbers in each time bin are large enough for statistically meaningful fits to be performed. Thanks to its high flux, we managed to divide the whole data set (0-30 s) into 62 time bins. We find that the data in each time bin can be well fit by a BB+PL model, and that the BB temperature evolves with time. The fitting results are presented in Table 2 and Fig.10. The time-integrated spectrum, however, cannot be fit with such a model ($\chi^2/\text{dof} = 14732/276$). A Band+PL model gives a much improved fit, although the fit is still not statistically acceptable ($\chi^2/\text{dof} = 2024/275$). The best fitting parameters are $\alpha = -0.83$, $\beta = -3.68$, $E_p = 847$ keV, and $\Gamma = -1.85$. Notice that the high energy photon index of the time-integrated Band spectrum is much steeper/softer than that observed in typical GRBs (Fig.19).

In Fig.20, we display the lightcurves of both the thermal and the power-law components. It is found that the two components in general track each other. This suggests that the physical origins of the two components are related to each other (see Section 5 for more discussion).

An important inference from the analysis of GRB 090902B is that a Band-like spectrum can be a result of temporal superposition of many blackbody-like components. This raises the interesting possibility of whether all “Band” function spectra are superposed thermal spectra. From the comparison between GRB 090902B and GRB 080916C (Fig.18), we find that such speculation is far-fetched. As discussed above, GRB 080916C shows no evidence of “narrowing” as the time bin becomes small (~ 1 s in the rest frame). In the case of GRB 090902B, a clear “narrowing” feature is seen. For the time integrated spectrum, GRB 080916C has a wide Band function (with $\alpha \sim -1.0$, $\beta \sim -2.27$), while GRB 090902B (0-20 s) has a narrow Band function (with $\alpha = -0.58$, $\beta = -3.32$) with worse reduced χ^2 . Another difference between GRB 090902B and GRB 080916C is that the former has a PL component, which leverages the BB spectrum on both the low-energy and the high-energy ends to make a BB spectrum look more similar to a (narrow) Band function. GRB 080916C does not have such a component, and the Band component covers the entire *Fermi* energy range (GBM & LAT). We therefore conclude that GRB 090902B is a special case, whose spectrum may have a different origin from GRB 080916C (and probably most other LAT GRBs as well, see Sect.3.5 below).

3.4. GRB 090926A

This is another bright long GRB with a duration ~ 20 s. In our analysis, the lightcurve is divided into 9 segments. The Band function gives an acceptable fit to all the time bins (Fig.11). We however notice a flattening of β after ~ 11 s after the trigger. Also the Band function fit gives a worse reduced χ^2 (although still acceptable) after this epoch. Since our data analysis strategy is to go for the simplest models, we do not explore more complicated models that invoke Band + PL or Band + CPL (as is done by the Fermi team, Abdo et al. 2010b). In any case, our analysis does not disfavor the possibility that a new spectral component emerges after ~ 11 s since the trigger (Abdo et al. 2010b).

3.5. Other GRBs

The time resolved spectra of other 13 GRBs are all adequately described by the Band function, similar to GRB 080916C. The Band-function spectral parameters are generally similar to GRB 080916C. It is likely that these GRBs join GRB 080916C forming a “Band-only” type GRBs. In the current sample of 17 GRBs, only GRB 090510, GRB 090902B and probably GRB 090926A do not belong to this category and have an extra PL component extending to high energies. One caveat is that some GRBs in the sample are not very bright, so that we only managed to divide the lightcurves into a small number of time bins (e.g. 3 bins for GRB 080825C, 1 bin for GRB 081024B, 3 bins for GRB 090328, 3 bins for GRB 091031, 2 bins for GRB 100225A, and 1 bin for GRB 100325A). So one cannot disfavor the possibility that the observed spectra are superposition of narrower components (similar to GRB 090902B). However, at comparable time resolution, GRB

090902B already shows features that are different from these GRBs: (1) the Band component is “narrower”, and (2) there is an extra PL component. These two features are not present in other GRBs. We therefore suggest that most LAT/GBM GRBs are similar to GRB 080916C.

3.6. Spectral parameter distributions

Since the time-resolved spectra of most GRBs in our sample can be adequately described as a Band function, we present the distributions of the Band function parameters in this section. Since their MeV component may be of a different origin, GRB 090510 and GRB 090902B are not included in the analysis.

The distributions of the spectral parameters α , β , and E_p are presented in Figure 19, with a comparison with those of the bright BATSE GRB sample (Preece et al. 2000). It is found that the distributions peak at $\alpha = -0.9$, $\beta = -2.6$, and $E_p \sim 781$ keV, respectively. The α and β distributions are roughly consistent with those found in the bright BATSE GRB sample (Preece et al. 2000). The E_p distribution of the current sample has a slightly higher peak than the bright BATSE sample (Preece et al. 2000). This is likely due to a selection effect, namely, a higher E_p would favor GeV detections.

3.7. Spectral parameter correlations

For time-integrated spectra, it was found that E_p is positively correlated with the isotropic gamma-ray energy and the isotropic peak gamma-ray luminosity (Amati et al. 2002; Wei & Gao 2003; Yonetoku et al. 2004). For time resolved spectra, E_p was also found to be generally correlated with flux (and therefore luminosity, Liang et al. 2004), although in individual pulses, both a decreasing E_p pattern and a E_p -tracking-flux pattern have been identified (Ford et al. 1995; Liang & Kargatis 1996; Kaneko et al. 2006; Lu et al. 2010).

In Fig.21, we present the E_p -luminosity relations. Fig.21a is for the global $E_p - L_{\gamma,iso}^p$ correlation. Seven GRBs in our sample that have redshift information (and hence, the peak luminosity) are plotted against previous GRBs (a sample presented in Zhang et al. 2009). Since the correlation has a large scatter, all the GBM/LAT GRBs follow the same correlation trend. In particular, GRB 090902B, whose E_p is defined by the BB component, also follows a similar trend. This suggests that even if there may be two different physical mechanisms to define a GRB’s E_p , both mechanisms seem to lead to a broad $E_p - L_{\gamma,iso}^p$ relation. It is interesting to note that the short GRB 090510 (the top yellow point), even located at the upper boundary of the correlation, is still not an outlier. This is consistent with the finding (Zhang et al. 2009; Ghirlanda et al. 2009) that long/short GRBs are not clearly distinguished in the $L_{\gamma,iso}^p - E_p$ domain.

In Fig.21b, we present the internal $E_p - L_{\gamma,iso}$ correlation. It is interesting to note that although

with scatter, the general positive correlation between E_p and $L_{\gamma,\text{iso}}$ as discovered by Liang et al. (2004) clearly stands. More interestingly, the BB-defined E_p (in GRB 090902B) follows a similar trend to the Band-defined E_p (e.g. in GRB 080916C and GRB 090926A), although different bursts occupy a different space region in the $E_p - L_{\gamma,\text{iso}}$ plane.

In Fig.22, we present various pairs of spectral parameters in an effort to search for possible new correlations. The GRBs with redshift measurements are marked in colors, while those without redshifts are marked in gray with an assumed redshift $z = 1$. In order to show the trend of evolution, points for same burst are connected, with the beginning of evolution marked as a circle.

No clear correlation pattern is seen in the $E_p - \alpha$ and $E_p - \beta$ plots. Interestingly, a preliminary trend of correlation is found in the following two domains.

- An $\alpha - \beta$ anti-correlation: Fig.22a shows a rough anti-correlation between α and β in individual GRBs. This suggests that a harder α corresponds to a softer β , suggesting a narrower Band function. In the time domain, there is evidence in some GRBs (e.g. GRB 080916C, GRB 090926A, and GRB 100414A, see Figs.2,11,17) that the Band function “opens up” as time goes by, but the opposite trend is also seen in some GRBs (e.g. GRB 091031, Fig.13). The linear Pearson correlation coefficients for individual bursts are insert in Fig.22a
- A flux- α correlation: Fig.22b shows a rough correlation between flux and α . Within the same burst, there is rough trend that as the flux increases, α becomes harder. The linear Pearson correlation coefficients for individual bursts are presented in Fig.22b inset. One possible observational bias is that when flux is higher, one tends to get a smaller time slice based on the minimum spectral analysis criterion. If the time smearing effect can broaden the spectrum, then a smaller time slice tends to give a narrower spectrum, and hence, a harder α . This would be relevant to bursts similar to GRB 090902B, but not bursts similar to GRB 080916C (which does not show spectral evolution as the time resolution becomes finer). More detailed analyses of bright GRBs can confirm whether such a correlation is intrinsic or due to the time resolution effect discussed above.

Several caveats should be noted for these preliminary correlations: First, some bursts do not obey these correlations, so the correlations, if any, are not universal; Second, the currently chosen time bins are based on the requirement for adequate spectral analyses, so the time resolution varies in different bursts. For some bright bursts, a burst pulse can be divided into several time bins, while in some faint others, a time bin corresponds to the entire pulse; Third, the current sample is still too small. A time-resolved spectral analysis for more bright GBM GRBs may confirm or dispute these correlations.

4. Elemental Spectral Components and their physical origins

4.1. Three phenomenologically identified elemental spectral components

The goal of our time-resolved spectral analysis is to look for “elemental” emission units that shape the observed GRB prompt gamma-ray emission. In the past it has been known that time-integrated GRB spectra are mostly fit by the Band function (Band et al. 1993). However, whether this function is an elemental unit in the time-resolved spectra is not known. One speculation is that this function is the superposition of many simpler emission units. If such a superposition relies on adding the emission from many time slices, then these more elemental units should show up as the time bins become small enough.

One interesting finding of our time-resolved spectral analyses is that the “Band”-like spectral component seen in GRB 090902B is different from that seen in GRB 080916C and some other Band-only GRBs. While the Band spectral indices of GRB 080916C essentially do not change as the time bins become progressively smaller, that of GRB 090902B indeed show the trend of “narrowing” as the time bin becomes progressively smaller. With the finest spectral resolution, GRB 090902B spectra can be fit by the superposition of a PL component and a CPL function, including a Planck function. Even for the time-integrated spectrum, the “Band”-like component in GRB 090902B appears “narrower” than that of GRB 080916C. All these suggest that the “Band”-like component of GRB 090902B is fundamentally different from that detected in GRB 080916C and probably also other Band-only GRBs³. Similarly, the time-resolved spectra of the short GRB 090510 can be well fit by the superposition of a PL component and a CPL spectrum (although not a Planck function). The PL component extends to high energies with a positive slope in νF_ν . The CPL component may be modeled as a multi-color blackbody spectrum. We therefore speculate that the MeV component of GRB 090510 is analogous to that of GRB 090902B.

Phenomenologically, the power law component detected in GRB 090902B and GRB 090510 is an extra component besides the Band-like component. Such a component may have been also detected in the BATSE-EGRET burst GRB 941017 (González et al. 2003), and may also exist in GRB 090926A at later epochs.

We therefore speculate that phenomenologically there might be three elemental spectral components that shape the prompt gamma-ray spectrum. These include: (I) a *Band function component* (“Band” in abbreviation) that covers a wide energy range (e.g. 6-7 orders of magnitude in GRB 080916C) and persists as the time bins become progressively smaller. It shows up in GRB 080916C and 13 other LAT GRBs; (II) a *quasi-thermal component* (“BB” in abbreviation⁴) which becomes

³Our finest time interval is around 1s in the rest frame of the burst. Theoretically, how time-integrated spectra broaden with increasing time bins is subject further study. Our statement is therefore relevant for time resolution longer than 1s.

⁴Notice that the abbreviation “BB” here not only denotes blackbody, but also includes various modifications to

progressively narrower as the time bin becomes smaller, and eventually can be represented as a blackbody (or multi-color blackbody) component as seen in GRB 090902B; (III) a *power law component* (“PL” in abbreviation) that extends to high energy as seen in GRBs 090902B and 090510, which has a positive slope in the νF_ν spectrum and should have an extra peak energy (E_p) at an even higher energy that is not well constrained by the data.

Figure 23 is a cartoon picture of the νF_ν spectrum that includes all three phenomenologically identified elemental spectral components. The time resolved spectra of the current sample can be understood as being composed of one or more of these components. For example, GRB 080916C and other 13 GRBs have Component I (Band), GRB 090902B and probably GRB 090510 have Components II (BB) and III (PL), and GRB 0900926A has Component I initially, and may have components I and III at later times.

4.2. Possible physical origins of the three spectral components

4.2.1. Band Component

The fact that this component extends through a wide energy range (e.g. 6-7 orders of magnitude for GRB 080916C) strongly suggests that a certain non-thermal emission mechanism is in operation. This demands the existence of a population of power-law-distributed relativistic electrons, possibly accelerated in internal shocks or in regions with significant electron heating, e.g. magnetic dissipation. In the past there have been three model candidates for prompt GRB emission: synchrotron emission, synchrotron self-Compton (SSC), and Compton upscattering of a thermal photon source. In all these models the high energy PL component corresponds to emission from a PL-distributed electron population. The spectral peak energy E_p may be related to the minimum energy of the injected electron population, an electron energy distribution break, or the peak of the thermal target photons.

Most prompt emission modeling (Mészáros et al. 1994; Pilla & Loeb 1998; Pe’er & Waxman 2004a; Razzaque et al. 2004; Pe’er et al. 2006; Gupta & Zhang 2007) suggest that the overall spectrum is curved, including multiple spectral components. Usually a synchrotron component is accompanied by a synchrotron self-Compton (SSC) component. For matter-dominated fireball models, one would expect the superposition of emissions from the photosphere and from the internal shock dissipation regions. As a result, the fact that 14/17 ($\sim 80\%$) of GRBs in our sample have a Band-only spectrum is intriguing. The three theoretically expected spectral features, i.e. the quasi-thermal photosphere emission, the SSC component (if the MeV component is of synchrotron origin), and a pair-production cutoff at high energies, are all not observed. This led to the suggestion that the outflows of these GRBs are Poynting flux dominated (Zhang & Pe’er 2009). Within such a

the blackbody spectrum such as multi-color blackbody.

picture, the three missing features can be understood as the following: (1) Since most energy is carried in magnetic fields and not in photons, the photosphere emission (BB component) is greatly suppressed; (2) Since the magnetic energy density is higher than the photon energy density, the Compton Y parameter is smaller than unity, so that the SSC component is naturally suppressed; (3) A Poynting flux dominated model usually has a larger emission radius than the internal shock model (Lyutikov & Blandford 2003 for current instability and Zhang & Yan 2011 for collision-induced magnetic reconnection/turbulence). This reduces the two-photon annihilation opacity and increases the pair cutoff energy. This allows the Band component extend to very high energy (e.g. 13.2 GeV for GRB 080916C).

Another possibility, advocated by Beloborodov (2010) and Lazzati & Begelman (2010) in view of the *Fermi* data (see also discussion by Thompson 1994; Rees & Mészáros 2005; Pe’er et al. 2006; Giannios & Spruit 2007; Fan 2009; Toma et al. 2010; and Ioka 2010), is that the Band component is the emission from a dissipative photosphere. This model invokes relativistic electrons in the regions where Thomson optical depth is around unity, which upscatter photosphere thermal photons to high energies to produce a power law tail. This model can produce a Band-only spectrum, but has two specific limitations. First, the high energy power law component cannot extend to energies higher than GeV in the cosmological rest frame, since for effective upscattering, the emission region cannot be too far above the photosphere. The highest photon energy detected in GRB 080916C is 13.2 GeV (which has a rest-frame energy ~ 70 GeV for its redshift $z = 4.35$). This disfavors the dissipative photosphere model. This argument applies if the LAT-band photons are from the same emission region as the MeV photons, as suggested by the single Band function spectral fits. It has been suggested that the LAT emission during the prompt phase originates from a different emission region, e.g. the external shock (Kumar & Barniol Duran 2009; Ghisellini et al. 2010). This requires that the two distinct emission components conspire to form a nearly featureless Band spectrum in all temporal epochs, which is contrived. As will be shown in Sect.5.2 later, there is compelling evidence that the LAT emission during the prompt emission phase is of an internal origin. In particular, the peak of the GeV lightcurve of GRB 080916C coincides with the second (the brightest) peak of GBM emission, and the 13.2 GeV photon coincides with another GBM lightcurve peak. All these suggest an internal origin of the GeV emission during the prompt phase.

The second limitation of the dissipative photosphere model is that the photon spectral index below E_p is not easy to reproduce. The simplest blackbody model predicts a Rayleigh-Jeans spectrum $\alpha = +1$. By considering slow heating, this index can be modified as $\alpha = +0.4$ (Beloborodov 2010). Both are much harder from the observed $\alpha \sim -1$ value. In order to overcome this difficulty, one may appeal to the superposition effect, i.e. the observed Band spectrum is the superposition of many fundamental blackbody emission units (e.g. Blinnikov et al. 1999; Toma et al. 2010; Mizuta et al. 2010; Pe’er & Ryde 2010). However, no rigorous calculation has been performed to fully reproduce the $\alpha = -1$ spectrum. Pe’er & Ryde (2010) show that when the central engine energy injection is over and the observed emission is dominated by the high-latitude emission, an $\alpha = -1$ can be reproduced with the flux decaying rapidly with $\propto t^{-2}$. During the phase when the

central engine is still active, the observed emission is always dominated by the contribution along the line of sight, which should carry the hard low energy spectral index of the blackbody function. Observationally, the Band component spectral indices are not found to vary when the time bins are reduced (in stark contrast to the narrow Band-like component identified in GRB 090902B). This suggests that at least the temporal superposition of many blackbody radiation units is not the right interpretation for this component.

4.2.2. *Quasi-Thermal (BB) Component*

The MeV component in GRB 090902B narrows with reduced time resolution and eventually turns into being consistent with a blackbody (or multi-color blackbody) as the time bin becomes small enough. This suggests a thermal origin of this component. Within the GRB content, a natural source is the emission from the photosphere where the photons advected in the expanding relativistic outflow turn optically thin for Compton scattering. In fact, the original fireball model predicts a quasi-thermal spectrum (Paczýnski 1986; Goodman 1986). In the fireball shock model, such a quasi-blackbody component is expected to be associated with the non-thermal emission components (Mészáros & Rees 2000; Mészáros et al. 2002; Daigne & Mochkovitch 2002; Pe’er et al. 2006).

Some superposition effects may modify the thermal spectrum to be different from a pure Planck function. The first is the temporal smearing effect. If the time bin is large enough, one samples photosphere emission from many episodes, and hence, the observed spectrum should be a multi-color blackbody. This effect can be diminished by reducing the time bin for time-resolved spectral analyses. GRB 090902B is such an example. The second effect is inherited in emission physics of relativistic objects. At a certain epoch, the observer detects photons coming from different latitudes from the line of sight, with different Doppler boosting factors. The result is an intrinsic smearing of the Planck function spectrum. Pe’er & Ryde (2010) have shown that after the central engine activity ceases, the high-latitude emission effect would give an $\alpha \sim -1$ at late times, with a rapidly decaying flux $F_\nu \propto t^{-2}$. This second superposition effect is intrinsic, and cannot be removed by reducing the time bins.

The case of the thermal component is most evidenced in GRB 090902B, and probably also in GRB 090510. In both bursts, the MeV component can be well fit with a CPL + PL spectrum. The exponential cutoff at the high energy end is consistent with thermal emission with essentially no extra dissipation. For GRB 090902B, the low energy spectral index Γ_{CPL} is typically ~ 0 , and can be adjusted to +1 (blackbody). For GRB 090510, Γ_{CPL} is softer (~ -0.7). Since it is a short GRB, the high-latitude effect may be more important. The softer low energy spectral index may be a result of the intrinsic high-latitude superposition effect (Pe’er & Ryde 2010).

4.2.3. Power-Law (PL) Component

This component is detected in GRB 090902B and GRB 090510. Several noticeable properties of this component are: (1) For our small sample, this component is always accompanied by a low energy MeV component (likely the BB component). Its origin may be related to this low energy component; (2) It is demanded in both the low energy end and the high energy end, and amazingly the same spectral index can accommodate the demanded excesses in both ends. This suggests that either this PL component extends for 6-7 orders of magnitude in energy, or that multiple emission components that contribute to the excesses in both the low and high energy regimes have to coincide to mimic a single PL; (3) The spectral slope is positive in the νF_ν space, so that the main energy power output of this component is at even higher energies (possibly near or above the upper bound of the LAT band).

Since the non-thermal GRB spectra are expected to be curved (Mészáros et al. 1994; Pilla & Loeb 1998; Pe’er & Waxman 2004a; Razzaque et al. 2004; Pe’er et al. 2006; Gupta & Zhang 2007; Asano & Terasawa 2009), the existence of the PL component is not straightforwardly expected. It demands coincidences of various spectral components to mimic a single PL component in the low and high energy ends. Pe’er et al. (2010) have presented a theoretical model of GRB 090902B. According to this model, the apparent PL observed in this burst is the combination of the synchrotron emission component (dominant at low energies), the SSC and Comptonization of the thermal photons (both dominant at high energies). A similar model was analytically discussed by Gao et al. (2009) within the context of GRB 090510.

One interesting question is how Component III (PL) differs from Component I (Band). Since both components are non-thermal, they may not be fundamentally different. They can be two different manifestations of some non-thermal emission mechanisms (e.g. synchrotron and inverse Compton scattering) under different conditions. On the other hand, since Component III seems to be associated with Component II (BB) (e.g. in GRB 090902B and GRB 090510), its origin may be related to Component II. One possible scenario is that Component III (at least the part above component II) is the Compton-upscattered emission of Component II (e.g. Pe’er & Waxman 2004b for GRB 941017). The fact that the lightcurves of the BB component and the PL component of GRB 090902B roughly track each other (Fig.20) generally supports such a possibility. Within this interpretation, one must attribute the PL part below the thermal peak as due to a different origin (e.g. synchrotron, see Pe’er et al. 2010). Alternatively, Component I and III may be related to non-thermal emission from two different emission sites (e.g. internal vs. external or two different internal locations). Indeed, if the late spectra of GRB 090926A are the superposition of the components I and III, then both components can coexist, which may correspond to two different non-thermal emission processes and/or two different emission sites.

4.3. Possible Spectral Combinations of GRB Prompt Emission

Using the combined GBM and LAT data, we have phenomenologically identified three elemental spectral components during the prompt GRB phase (Fig.23). Physically they may have different origins (see above). One may speculate that all the GRB prompt emission spectra may be decomposed into one or more of these spectral components. It is therefore interesting to investigate how many combinations are in principle possible, how many have been discovered, how many should not exist and why, and how many should exist and remain to be discovered. We discuss the following possibilities in turn below (see Fig.24 for illustrations).

1. Component I (Band) only:

This is the most common situation, which is observed in 14/17 GRBs in our sample exemplified by GRB 080916C. Either the BB and PL components do not exist, or they are too faint to be detected above the Band component. If the BB component is suppressed, these bursts may signify non-thermal emission from an Poynting flux dominated flow.

2. Component II (BB) only:

No such case exists in the current sample. GRB 090902B, and probably also GRB 090510, have a BB component, but it is accompanied by a PL component in both GRBs. It remains to be seen whether in the future a BB-only GRB will be detected, or whether a BB component is always accompanied by a PL component. Since the case of GRB 090902B is rare, we suspect that the BB-only GRBs are even rarer, if they exist at all.

3. Component III (PL) only:

Our PL component stands for the high energy spectral component seen in GRB 090902B and GRB 090510, which likely has a high E_p near or above the boundary of the LAT band. Observationally, there is no solid evidence for such PL-only GRBs⁵. In our current sample which covers the widest energy band, the PL component only exists in 2 out of 17 GRBs, and is found to be associated with the BB component. The luminosity of the PL component is found to roughly track that of the thermal component (Fig.20). If the PL component is the Comptonization of a low energy photon source (e.g. the BB component), then PL-only GRBs may not exist in nature.

4. I + II:

⁵Most of Swift GRBs can be fit with a PL (Sakamoto et al. 2008). However, this is due to the narrowness of the energy band of the gamma-ray detector BAT on board Swift. The E_p of many Swift GRBs are expected to be located outside the instrument band. In fact, using a Band function model and considering the variation of E_p within and outside the BAT band, one can reproduce the apparent hardness of Swift GRBs, and obtain an effective correlation between the BAT-band photon index and E_p (e.g. Zhang et al. 2007; Sakamoto et al. 2009). If a GRB is observed in a wider energy band, the spectrum should be invariably curved.

Such a case is not found in our sample. If the Band component is the emission from the internal shocks and the BB component is the emission from the photosphere, then such a combination should exist and be common for fireball scenarios. An identification of such a case would confirm the non-thermal nature of the Band component (since the thermal component is manifested as the BB component). Observationally, an X-ray excess has been observed in 12 out of 86 ($\sim 14\%$) bright BATSE GRBs (Preece et al. 1996). This could be due to the contamination of a BB component in the X-ray regime. With the excellent spectral coverage of *Fermi*, we expect that such a spectral combination may be identified in some GRBs, even if technically it may be difficult because there are too many spectral parameters to constrain.

5. I + III:

Such a combination has not been firmly identified in our sample. Nonetheless, the spectral hardening of GRB 090926A after 11 s may be understood as the emergence of the PL component on top of the Band component seen before 11 s. Physically it may be related to two non-thermal spectral components or non-thermal emission from two different regions.

6. II + III:

Such a case is definitely identified in GRB 090902B, and likely in GRB 090510 as well. From the current sample, it seems that such a combination is not as common as the Band-only type, but nonetheless forms a new type of spectrum that deserves serious theoretical investigations. Physically, the high-energy PL component is likely the Compton up-scattered emission of the BB component, although other non-thermal processes (e.g. synchrotron and SSC) could also contribute to the observed emission (Pe’er et al. 2010).

7. I + II + III:

The full combination of all three spectral components (e.g. Fig.23) is not seen from the current sample. In any case, in view of the above various combinations (including speculative ones), one may assume that the full combination of the three spectral components is in principle possible. Physically this may correspond to one photosphere emission component and two more non-thermal components (either two spectral components or non-thermal emission from two different regions). Nonetheless, technically there are too many parameters to constrain, so that identifying such a combination is difficult.

5. LAT-band emission vs. GBM-band emission

Besides the joint GBM/LAT spectral fits, one may also use temporal information to investigate the relationship between the emission detected in the GBM-band and that detected in the LAT band. In this section we discuss three topics: delayed onset of LAT emission, rough tracking behavior between GBM and LAT emissions, and long-lasting LAT afterglow.

5.1. Delayed onset of LAT emission

The *Fermi* team has reported the delayed onset of LAT emission in several GRBs (GRBs 080825C, 080916C, 090510, 090902B, Abdo et al. 2009a,b,c,d). Our analysis confirms all these results. In Table 1, we mark all the GRBs in our sample that show the onset delay feature.

There have been several interpretations to the delayed onset of GeV emission discussed in the literature. Toma et al. (2009) suggested that GeV emission is the upscattered cocoon emission by the internal shock electrons. Razzaque et al. (2009) interpreted the GeV emission as the synchrotron emission of protons. Since it takes a longer time for protons to be accelerated and be cooled to emit GeV photons, the high energy emission is delayed. Li (2010b) interpreted GeV emission as the upscattered prompt emission photons by the residual internal shocks.

Although it is difficult to test these models using the available data, our results give some observational constraints to these models. First, except GRBs 090510 and 090902B whose GeV emission is a distinct spectral component, other GRBs with onset delay still have a simple Band-function spectrum after the delayed onset. This suggests that for those models that invoke two different emission components to interpret the MeV and GeV components, one needs to interpret the coincidence that the GeV emission appears as the natural extension of the MeV emission to the high energy regime.

For such delayed onsets whose GeV and MeV emissions form the same Band component, one may speculate two simpler explanations. One is that there might be a change in the particle acceleration conditions (e.g. magnetic configuration in the particle acceleration region). As shown in Sect.3.1, the early spectrum during the first time bin (before onset of LAT emission) of GRB 080916C may be simply a consequence of changing the electron spectral index. One may speculate that early on the particle acceleration process may not be efficient, so that the electron energy spectral index is steep. After a while (the observed delay), the particle acceleration mechanism becomes more efficient, so that the particle spectral index reaches the regular value. The second possibility is that there might be a change in opacity. The GBM data alone during the first time bin gives a similar β as later epochs. It is possible that there might be a spectral cutoff slightly above the GBM band early on. A speculated physical picture would be that the particle acceleration conditions are similar throughout the burst duration, but early on the pair production opacity may be large (probably due to a lower Lorentz factor or a smaller emission radius), so that the LAT band emission is attenuated. The opacity later drops (probably due to the increase of Lorentz factor or the emission radius), so that the LAT band emission can escape from the GRB. Within such a scenario, one would expect to see a gradual increase of maximum photon energy as a function of time. Figure 25 shows the LAT photon arrival time distribution of GRB 080916C. Indeed one can see a rough trend of a gradual increase of the maximum energy with time.

One last possibility is that the LAT band emission is dominated by the emission from the external shock, which is delayed with respect to the GBM-band prompt emission. This possibility is discussed in more detail below in Sec. 5.3.

5.2. Rough tracking behavior

Inspecting the multi-band lightcurves (Figs.1-17 left panels), for bright GRBs (e.g. 080916C, 090217, 090323, 090902B) the LAT emission peaks seem to roughly track some peaks of the GBM emission (aside from the delayed onset for some of them). For example, the peak of the LAT lightcurve of GRB 080916C coincides with the second GBM peak. This is consistent with the spectral analysis showing that most time-resolved joint spectra are consistent with being the same (Band-function) spectral component. Even for GRB 090902B whose LAT band emission is from a different emission component from the MeV BB component, the emissions in the two bands also roughly track each other (Fig.20). This suggests that the two physical mechanisms that power the two spectral components are related to each other.

The rough tracking behavior is evidence against the proposal that the entire GeV emission is from the external forward shock (see Sec. 5.3 for more discussion). Within the forward shock model, the fluctuation in energy output from the central engine should be greatly smeared, since the observed flux change amplitude is related to $\Delta E/E \ll 1$ (where E is the total energy already in the balstwave, and ΔE is the newly injected energy from the central engine), rather than ΔE itself within the internal models.

5.3. Long Term Emission in the LAT Band

In order to study the long-term lightcurve behavior, we extract the GBM-band and LAT-band lightcurves in logarithmic scale and present them in the bottom right panel of Figs.1-17. We unevenly bin the LAT lightcurves with bin sizes defined by the requirement that the signal-to-noise ratio must be > 5 . For a close comparison, we correspondingly re-bin the GBM lightcurves using the same bin sizes. Some GRBs (e.g. 080916C, 090510, 090902B, and 090926A) have enough photons to make a well sampled LAT lightcurve.

In several GRBs, LAT emission lasts longer than GBM emission and decays as a single power law (Ghisellini et al. 2010). The decay indices of LAT emission are marked in the last panel of Figs.1-17, which can be also found in Table 3. Due to low photon numbers, it is impossible to carry out a time resolved spectral analysis. In any case, the LAT-band photon indices of long-term LAT emission are estimated and also presented in Table 3. In Table 1 we mark those GRBs with detected LAT emission longer than GBM emission and those without. The most prominent ones with long lasting LAT afterglow are GRBs 080916C, 090510, 090902B, and 090926A. Spectral analyses suggest that the LAT emission in GRBs 090510 and 090902B is a different spectral component from the MeV emission. The GBM lightcurves of these GRBs indeed follow a different trend by turning off sharply as compared with the extended PL decay in the LAT band. GRB 090926A, on the other hand, shows a similar decay trend in both GBM and LAT bands. GRB 080916C is special. Although the spectral analysis shows a single Band function component, the GBM lightcurve turns over sharply around 70-80 seconds, while the LAT emission keeps decaying with a single PL.

One caveat of LAT long-term lightcurves is that they depend on the level of background and time-bin selection. Due to the low count rate at late times, the background uncertainty can enormously change the flux level, and a different way of binning the data may change the shape of the lightcurve considerably. In our analysis, the background model is extracted from the time interval prior to the GBM trigger in the same sky region that contains the GRB. The bin-size is chosen to meet the 5σ statistics to reduce the uncertainty caused by arbitrary binning.

Our data analysis suggests a controversial picture regarding the origin of this GeV afterglow. Spectroscopically, the LAT-band emission is usually an extension of the GBM-band emission and forms a single Band-function component, suggesting a common physical origin with the GBM-band emission. If one focuses on the prompt emission lightcurves, the LAT-band activities seem to track the GBM-band activities. Even for GRB 090902B which shows a clear second spectral component, the PL component variability tracks that of the BB component well (Fig.20), suggesting a physical connection between the two spectral components. These facts tentatively suggest that at least during the prompt emission phase, the LAT-band emission is likely connected to the GBM-band emission, and may be of an “internal” origin similar to the GBM-band emission.

It has been suggested that the entire GeV emission originates from the external shock (e.g. Kumar & Barniol Duran 2009a, 2009b; Ghisellini et al. 2010; Corsi et al. 2009). This idea is based on the power law temporal decay law that follows the prompt emission. Such a GeV afterglow scenario is not straightforwardly expected for the following reasons. First, before *Fermi*, afterglow modeling suggests that for typical afterglow parameters, the GeV afterglow is initially dominated by the synchrotron self-Compton component (Mészáros & Rees 1994; Dermer et al. 2000; Zhang & Mészáros 2001; Wei & Fan 2007; Gou & Mészáros 2007; Galli & Piro 2007; Yu et al. 2007; Fan et al. 2008), or by other IC processes invoking both forward and reverse shock electrons (Wang et al. 2001). For very energetic GRBs such as GRB 080319B, one may expect a synchrotron-dominated afterglow all the way to an energy ~ 10 GeV (Zou et al. 2009; Fan et al. 2008). Second, the required parameters for the external shock are abnormal to interpret the data. For example, the magnetic field strength at the forward shock needs to be much smaller than equipartition, consistent with simply compressing the ISM magnetic field without shock amplification (Kumar & Barniol Duran 2010). This, in turn, causes a problem in accelerating electrons to a high enough energy to enable emission of GeV photons (Li 2010a; Piran & Nakar 2010). Moreover, the circumburst number density of these long GRBs are required to be much lower than that of a typical ISM (e.g., Kumar & Barniol Duran 2010), which challenges the collapsar model. Finally, observed GeV decay slope is typically steeper than the predictions invoking a standard adiabatic forward shock (e.g. Figs.2,8,10,11,17, see also Ghisellini et al. 2010). One needs to invoke a radiative blastwave (Ghisellini et al. 2010) or a Klein-Nishina cooling-dominated forward shock (Wang et al. 2010) to account for the steepness of the decay slope.

The external shock model to interpret the entire GeV emission is challenged by the following two arguments. First, the GeV lightcurve peak coincides the second peak of the GBM lightcurve for GRB 080916C. This requires a fine-tuned bulk Lorentz factor of the fireball to make the deceleration

time coincide the epoch of the second central engine activity. This is highly contrived. Second, the external shock component should not have decayed steeply while the prompt emission is still on going. To examine this last point, we have applied the shell-blastwave code developed by Maxham & Zhang (2009) to model the blastwave evolution of GRB 080916C using the observed data by assuming that the outflow kinetic energy traces the observed gamma-ray lightcurve (assuming a constant radiation efficiency). The resulting LAT-band lightcurve always displays a shallow decay phase caused by refreshing the forward shock by materials ejected after the GeV lightcurve peak time even for a radiative blastwave, in stark contrast to the data. This casts doubts on the external shock origin of GeV emission during the prompt phase (Maxham et al. 2011). We note that detailed modeling of GRB 090510 (He et al. 2010) and GRB 090902B (Liu & Wang 2011) with the external shock model both suggests that the prompt GeV emission cannot be interpreted as the emission from the external forward shock.

Collecting the observational evidence and the theoretical arguments presented above, we suggest that at least during the prompt emission phase (when GBM-band emission is still on), the LAT-band emission is not of external forward shock origin.

After the GBM-band prompt emission is over, the LAT-band emission usually decays as a PL. We note that the long-term GeV lightcurve can be interpreted in more than one way. (1) If one accepts that the prompt GeV emission is of internal origin, one may argue that the external shock component sets in before the end of the prompt emission and thereafter dominates during the decay phase (Maxham et al. 2011). This requires arguing for coincidence of the same decaying index for the early internal and the late external shock emission. Considering a possible superposition effect (i.e. the observed flux during the transition epoch includes the contributions from both the internal and external shocks), this model is no more contrived than the model that interprets prompt GeV emission as from external shocks, which requires coincidence of internal emission spectrum and the external shock emission spectrum to mimic the same Band spectrum in all time bins (Kumar & Barniol Duran 2009). (2) An alternative possibility is to appeal to an internal origin of the entire GeV long-lasting afterglow, which reflects the gradual “die-off” of the central engine activity. The difficulty of such a suggestion is that it must account for the different decaying behaviors between the GBM-band emission and LAT-band emission in some (but not all) GRBs (e.g. GRB 080916C). To differentiate between these possibilities, one needs a bright GRB co-triggered by *Fermi* LAT/GBM and *Swift* BAT, so that an early *Swift* XRT lightcurve is available along with the early GeV lightcurve. The external-shock-origin GeV afterglow should be accompanied by a PL decaying early X-ray lightcurve (Liang et al. 2009) instead of the canonical steep-shallow-normal decaying pattern observed in most *Swift* GRBs (Zhang et al. 2006; Nousek et al. 2006; O’Brien et al. 2006). A violation of such a prediction would suggest an internal origin of the GeV afterglow.

6. Conclusions and discussion

We have presented a comprehensive joint analysis of 17 GRBs co-detected by *Fermi* GBM and LAT. We carried out a time-resolved spectral analysis of all the bursts with the finest temporal resolution allowed by statistics, in order to reduce temporal smearing of different spectral components. Our data analysis results can be summarized as the following:

- We found that the time-resolved spectra of 14 out of 17 GRBs are best modeled with the classical “Band” function over the entire *Fermi* spectral range, which may suggest a common origin for emissions detected by LAT and GBM. GRB 090902B and GRB 090510 are found to be special in that the data require the superposition between a MeV component and an extra power law component, and that the MeV component has a sharp cutoff above E_p . More interestingly, the MeV component of GRB 090902B becomes progressively narrower as the time bin gets smaller, and can be fit with a Planck function as the time bin becomes small enough. This is in stark contrast to GRB 080916C, which shows no evidence of “narrowing” with the reducing time bin. This suggests that the Band-function component seen in GRB 080916C is physically different from the MeV component seen in GRB 090902B.
- We tentatively propose that phenomenologically there can be three elemental spectral components (Fig.23), namely, (I): a Band-function component (Band) that extends to a wide spectral regime without “narrowing” with reduced time bins, which is likely of non-thermal origin; (II): a quasi-thermal component (BB) that “narrows” with reducing time bins and that can be reduced to a blackbody (or multi-color blackbody) function; and (III): a power-law component (PL) that has a positive slope in νF_ν space and extends to very high energy beyond the LAT energy band.
- Component I (Band) is the most common spectral component, which appears in 15 of 17 GRBs. Except GRB 090926A (which may have Component III at late times), all these GRBs have a Band-only spectrum in the time-resolved spectral analysis.
- Component II (BB) shows up in the time-resolved spectral analysis of GRB 090902B and possibly also in GRB 090510. The MeV component of these two GRBs can be fit with a power law with exponential cutoff (CPL). Since data demand the superposition with an additional PL component (Component III), the uncertainty in the spectral index of the PL component makes it possible to have a range of low energy photon indices for the CPL component. In particular, the MeV component of GRB 090902B can be adjusted to be consistent with a blackbody (Plank function). This is not possible for GRB 090510, whose low energy photon index is softer. In any case, the MeV component of GRB 090510 may be consistent with a multi-color blackbody.
- Component III (PL) shows up in both GRB 090902B and the short GRB 090510, and probably in the late epochs of GRB 090926A as well. It has a positive slope in νF_ν , which suggests

that most energy in this component is released near or above the high energy end of the LAT energy band.

- With the above three elemental emission components, one may imagine 7 possible spectral combinations. Most ($\sim 80\%$) of GRBs in our sample have the Band-only spectra. GRB 090902B has the BB+PL spectra in the time resolved spectral analyses, and GRB 090510 has a CPL + PL spectra. Both can be considered as the superposition between Components II and III. GRB 090926A may have the superposition between I and III at late epochs. Other combinations are not identified yet with the current analysis, but some combinations (e.g. I+II, I+II+III) may in principle exist.
- LAT-band emission has a delayed onset with respect to GBM-band emission in some (but not all) GRBs and it usually lasts much longer. In most cases (all except GRBs 090902B and 090510), however, the LAT and GBM photons are consistent with belonging to the same spectral component, suggesting a possible common origin. For bright bursts, the LAT-band activities usually roughly track the GBM-band activities. In the long-term, the LAT and GBM lightcurves sometimes (not always) show different decaying behaviors. The LAT lightcurves continuously decay as a power-law up to hundreds of seconds.
- A statistical study of the spectral parameters in our sample generally confirms the previously found correlations between E_p and luminosity, both globally in the whole sample and individually within each burst. We also discover preliminary rough correlations between α and β (negative correlation) and between flux and α (positive correlation). Both correlations need confirmation from a larger sample.

From these results, we can draw the following physical implications regarding the nature of GRBs.

The Band-only spectra are inconsistent with the simplest fireball photosphere-internal-shock model. This is because if the Band component is non-thermal emission from the internal shock, the expected photosphere emission should be very bright. A natural solution is to invoke a Poynting-flux-dominated flow. An alternative possibility is to interpret the Band component as the photosphere emission itself. However, the following results seem to disfavor such a possibility. (1) In some cases (e.g. GRB 080916C), the Band-only spectrum extends to energies as high as 10s of GeV; (2) The low-energy photon indices in the time-resolved spectra are typically -1 , much softer than that expected in the photosphere models; (3) There is no evidence that the Band component is the temporal superposition of thermal-like emission components in the Band-only sample. We therefore suggest that GRB 080916C and probably all Band-only GRBs may correspond to those GRBs whose jet composition is dominated by a Poynting flux rather than a baryonic flux (Zhang & Pe'er 2009; Zhang & Yan 2011).

The existence of a bright photosphere component in GRB 090902B (see also Ryde et al. 2010; Pe'er et al. 2010) suggests that the composition of this GRB is likely a hot fireball without strong

magnetization. It is rare, but its existence nonetheless suggests that GRB outflow composition may be diverse. Its associated PL component is hard to interpret, but it may be from the contributions of multiple non-thermal spectral components (Pe’er et al. 2010). The case of GRB 090510 may be similar to GRB 090902B. The low-energy spectral index of the MeV component is too shallow to be consistent with a blackbody, but the high-latitude emission from an instantaneously ejected fireball (which is relevant to short GRBs) would result in a multi-color blackbody due to the angular superposition effect (Pe’er & Ryde 2010).

The delayed onset of GeV emission may be simply due to one of the following two reasons: (1) The particle acceleration condition may be different throughout the burst. Initially, the electron spectral index may be steep initially (so that GeV emission is too faint to be detected), but later it turns to a shallower value so that GeV emission emerges above the detector sensitivity; (2) Initially the ejecta may be more opaque so that there was a pair-production spectral cutoff below the LAT band. This cutoff energy later moves to higher energies to allow LAT photons to be detected. Within this picture, the electron spectral index is similar throughout the burst. There are other models discussed in the literature to attribute GeV emission to a different origin from the MeV component. This is reasonable for GRB 090510 and GRB 090902B, but for most other GRBs this model is contrived since the GeV emission appears as the natural extension of the MeV Band-function to high energies.

The GeV emission during the prompt phase is very likely not of external forward shock origin. This is due to the following facts: (1) In most GRBs the entire *Fermi*-band emission is well fit by a single Band component. The GeV emission is consistent with being the extension of MeV to high energies. (2) During the prompt phase and except for the delayed onset in some GRBs, the LAT-band activities in bright GRBs generally track GBM-band activities. The latter property is relevant even for GRB 090902B which shows clearly two components in the spectra. (3) The peak of GeV lightcurve coincides the second peak of GBM lightcurve for GRB 080916C. A more reasonable possibility is that the GeV emission during the prompt phase has an “internal” origin similar to its MeV counterpart.

The origin of the long lasting GeV afterglow after the prompt emission phase (end of the GBM-band emission) is unclear. If it is from the external forward shock, one needs to introduce abnormal shock parameters, and to argue for coincidence to connect with the internal-origin early GeV emission to form a simple PL decay lightcurve. Alternatively, the long lasting GeV emission can be also of the internal origin. Future joint *Fermi*/*Swift* observations of the early GeV/X-ray afterglows of some bright GRBs will help to differentiate between these possibilities.

The two tentative correlations ($\alpha - \beta$ and α -flux) proposed in this paper need to be confirmed with a larger data sample, and their physical implications will be discussed then.

We thank Rob Preece for important instructions on *Fermi* data analysis. This work is partially supported by NASA NNX09AT66G, NNX10AD48G, and NSF AST-0908362 at UNLV. EWL, YZF,

and XFW acknowledge National Basic Research Program of China (973 Program 2009CB824800). This work is partially supported by the National Natural Science Foundation of China (grant 10873002 for EWL, and grants 10633040, 10921063 for XFW). EWL is also supported by Guangxi Ten-Hundred-Thousand project (Grant 2007201), Guangxi Science Foundation (2010GXNSFC013011), and the program for 100 Young and Middle-aged Disciplinary Leaders in Guangxi Higher Education Institutions. YZF is also supported by a special grant from Purple Mountain Observatory and by the National Nature Science Foundation of China (grant 11073057). XFW is also supported by the Special Foundation for the Authors of National Excellent Doctorial Dissertations of P. R. China by Chinese Academy of Sciences. AP is supported by the Riccardo Giacconi Fellowship award of the Space Telescope Science Institute.

REFERENCES

- Abdo, A. A., et al. 2009a, *Science*, 323, 1688
- Abdo, A. A., et al. 2009b, *Nature*, 462, 331
- Abdo, A. A., et al. 2009c, *ApJL*, 706, L138
- Abdo, A. A., et al. 2009d, *ApJ*, 707, 580
- Abdo, A. A., et al. 2010a, *ApJ*, 712, 558
- Ackermann, M. et al. 2010, *ApJ*, 716, 1178
- Akaike, H. 1974, *IEEE Transactions on Automatic Control*, 19, 716
- Amati, L., et al. 2002, *A&A*, 390, 81
- Ando, S., Nakar, E., & Sari, R. 2008, *ApJ*, 689, 1150
- Asano, K., & Terasawa, T. 2009, *ApJ*, 705, 1714
- Atwood, W. B., et al. 2009, *ApJ*, 697, 1071
- Band, D., et al. 1993, *ApJ*, 413, 281
- Barthelmy, S. D., et al. 2005, *ApJ*, 635, L133
- Beloborodov, A. M. 2010, *MNRAS*, 407, 1033
- Blinnikov, S. I., Kozyreva, A. V., & Panchenko, I. E. 1999, *Astron. Rep.*, 43, 739
- Corsi, A., Guetta, D., & Piro, L. 2010, *ApJ*, 720, 1008
- Cucchiara, A., Fox, D. B., Tanvir, N., & Berger, E. 2009a, *GRB Coordinates Network*, 9873, 1

- Cucchiara, A., Fox, D. B., Cenko, S. B., Tanvir, N., & Berger, E. 2009b, GRB Coordinates Network, Circular Service, 10031, 1
- Cucchiara, A., & Fox, D. B. 2010, GRB Coordinates Network, Circular Service, 10606, 1
- Daigne, F., & Mochkovitch, R. 2002, MNRAS, 336, 1271
- Dermer, C. D., & Mitman, K. E. 1999, ApJ, 513, L5
- Dermer, C. D., Chiang, J., & Mitman, K. E. 2000, ApJ, 537, 785
- Fan, Y.-Z. & Piran, T. 2008, Front. Phys. in China, 3, 306
- Fan, Y.-Z., Piran, T., Narayan, R., & Wei, D.-M. 2008, MNRAS, 384, 1483
- Fan, Y.-Z. 2009, MNRAS, 397, 1539
- Fan, Y.-Z. 2010, MNRAS, 403, 483
- Ford, L. A., et al. 1995, ApJ, 439, 307
- Galli, A., & Piro, L. 2007, A&A, 475, 421
- Gao, W.-H., Mao, J.-R., Xu, D., & Fan, Y.-Z. 2009, ApJ, 706, L33
- Gehrels, N. 1986, ApJ, 303, 336
- Ghirlanda, G., Nava, L., Ghisellini, G., Celotti, A., & Firmani, C. 2009, A&A, 496, 585
- Ghisellini, G., Ghirlanda, G., Nava, L., & Celotti, A. 2010, MNRAS, 403, 926
- Giannios, D., & Spruit, H. C. 2007, A&A, 469, 1
- Goldstein, A., & van der Horst, A. 2008, GRB Coordinates Network, 8245, 1
- Golenetskii, S., et al. 2009, GRB Coordinates Network, 9050, 1
- González, M. M., Dingus, B. L., Kaneko, Y., Preece, R. D., Dermer, C. D., & Briggs, M. S. 2003, Nature, 424, 749
- Goodman, J. 1986, ApJ, 308, L47
- Gou, L.-J., & Mészáros, P. 2007, ApJ, 668, 392
- Greiner, J., et al. 2009, A&A, 498, 89
- Gupta, N., & Zhang, B. 2007, MNRAS, 380, 78
- He, H.-N., Wu, X.-F., Toma, K., Wang, X.-Y., Mészáros, P. 2010, ApJ, submitted (arXiv:1009.1432)

- Hurley, K., et al. 1994, *Nature*, 372, 652
- Ioka, K. 2010, arXiv:1006.3073
- Kaneko, Y., Preece, R. D., Briggs, M. S., Paciesas, W. S., Meegan, C. A., & Band, D. L. 2006, *ApJS*, 166, 298
- Kaneko, Y., González, M. M., Preece, R. D., Dingus, B. L., & Briggs, M. S. 2008, *ApJ*, 677, 1168
- Kobayashi, S., Piran, T., & Sari, R. 1997, *ApJ*, 490, 92
- Kumar, P., & McMahon, E. 2008, *MNRAS*, 384, 33
- Kumar, P., & Barniol Duran, R. 2009, *MNRAS*, 400, L75
- Kumar, P., & Barniol Duran, R. 2010, *MNRAS*, in press (arXiv:0910.5726)
- Lazzati, D., & Begelman, M. C. 2009, *ApJ*, 700, L141
- Lazzati, D., & Begelman, M. C. 2010, arXiv:1005.4704
- Li, Z. 2010a, arXiv:1004.0791
- Li, Z. 2010b, *ApJ*, 709, 525
- Liang, E., & Kargatis, V. 1996, *Nature*, 381, 49
- Liang, E.-W., Dai, Z.-G., & Wu, X.-F. 2004, *ApJ*, 606, L29
- Liang, E.-W., Lü, H.-J., Hou, S.-J., Zhang, B.-B., & Zhang, B. 2009, *ApJ*, 707, 328
- Liu, R.-Y., & Wang, X.-Y. 2011, *ApJ*, in press (arXiv:1009.1289)
- Lu, R.-J., Hou, S.-J., & Liang, E.-W. 2010, *ApJ*, 720, 1146
- Lü H.-J. et al et al., 2010 , in prep.
- Lyutikov, M., & Blandford, R. 2003, arXiv:astro-ph/0312347
- Malesani, D., et al. 2009, *GRB Coordinates Network*, 9942, 1
- Maxham, A., & Zhang, B. 2009, *ApJ*, 707, 1623
- Maxham, A., Zhang, B.-B., & Zhang, B. 2011, *MNRAS*, submitted. (arXiv:1101.0144)
- Medvedev, M. V. 2000, *ApJ*, 540, 704
- Meegan, C., et al. 2009, *ApJ*, 702, 791
- Mészáros, P., & Rees, M. J. 1993, *ApJ*, 405, 278

- Mészáros, P., & Rees, M. J. 1994, MNRAS, 269, L41
- Mészáros, P., Rees, M. J., & Papathanassiou, H. 1994, ApJ, 432, 181
- Mészáros, P., & Rees, M. J. 2000, ApJ, 530, 292
- Mészáros, P., Ramirez-Ruiz, E., Rees, M. J., & Zhang, B. 2002, ApJ, 578, 812
- McEney, J., et al. 2008, GRB Coordinates Network, 8684, 1
- Mizuta, A., Nagataki, S., & Aoi, J. 2010, ApJL, submitted (arXiv:1006.2440)
- Nousek, J. A., et al. 2006, ApJ, 642, 389
- Ohno, M., et al. 2010, arXiv:1002.0228
- O’Brien, P. T., et al. 2006, ApJ, 647, 1213
- Paczynski, B. 1986, ApJ, 308, L43
- Panaitescu, A., & Mészáros, P. 2000, ApJ, 544, L17
- Pe’er, A., & Waxman, E. 2004a, ApJ, 613, 448
- Pe’er, A., & Waxman, E. 2004b, ApJ, 603, L1
- Pe’er, A., Mészáros, P., & Rees, M. J. 2005, ApJ, 635, 476
- Pe’er, A., Mészáros, P., & Rees, M. J. 2006, ApJ, 642, 995
- Pe’er, A. 2008, ApJ, 682, 463
- Pe’er, A. et al., 2010, ApJ, submitted (arXiv:1007.2228)
- Pe’er, A., & Ryde, F. 2010, ApJ, submitted (arXiv:1008.4590)
- Pilla, R. P., & Loeb, A. 1998, ApJ, 494, L167
- Piran, T., & Nakar, E. 2010, arXiv:1003.5919
- Preece, R. D., Briggs, M. S., Pendleton, G. N., Paciesas, W. S., Matteson, J. L., Band, D. L., Skelton, R. T., & Meegan, C. A. 1996, ApJ, 473, 310
- Preece, R. D., Briggs, M. S., Malozzi, R. S., Pendleton, G. N., Paciesas, W. S., & Band, D. L. 2000, ApJS, 126, 19
- Preece, R. 2008, GRB Coordinates Network, 8678, 1
- Razzaque, S., Mészáros, P., & Zhang, B. 2004, ApJ, 613, 1072

- Razzaque, S., Dermer, C. D., & Finke, J. D. 2009, arXiv:0908.0513
- McBreen, S., et al. 2010, *A&A*, 516, A71 /
- Rees, M. J., & Mészáros, P. 1992, *MNRAS*, 258, 41P
- Rees, M. J., & Mészáros, P. 1994, *ApJL*, 430, L93
- Rees, M. J., & Mészáros, P. 2005, *ApJ*, 628, 847
- Ryde, F., et al. 2010, *ApJ*, 709, L172
- Sakamoto, T., et al. 2005, *ApJ*, 629, 311
- Sakamoto, T., et al. 2008, *ApJS*, 175, 179
- Sakamoto, T., et al. 2009, *ApJ*, 693, 922
- Tagliaferri, G., et al. 2005, *Nature*, 436, 985
- Thompson, C. 1994, *MNRAS*, 270, 480
- Toma, K., Wu, X.-F., & Mészáros, P. 2009, *ApJ*, 707, 1404
- Toma, K., Wu, X.-F., & Mészáros, P. 2010, *ApJ*, submitted (arXiv:1002.2634)
- van der Horst, A. J., & Connaughton, V. 2008, *GRB Coordinates Network*, 8141, 1
- Wang, X.-Y., Dai, Z.-G., & Lu, T. 2001, *ApJ*, 556, 1010
- Wang, X.-Y., He, H.-N., Li, Z., Wu, X.-F., & Dai, Z.-G. 2010, *ApJ*, 712, 1232
- Wei, D.-M., & Fan, Y.-Z. 2007, *Chinese Journal of Astronomy and Astrophysics*, 7, 509
- Wei, D.-M., & Gao, W.-H. 2003, *MNRAS*, 345, 743
- Yonetoku, D., Murakami, T., Nakamura, T., Yamazaki, R., Inoue, A. K., & Ioka, K. 2004, *ApJ*, 609, 935
- Yu, Y.-W., Liu, X.-W., & Dai, Z.-G. 2007, *ApJ*, 671, 637
- Zhang, B. 2007, *ChJAA*, 7, 1
- Zhang B., Mészáros P. 2004, *Int. J. Mod. Phys. A*, 19, 2385
- Zhang, B., & Mészáros, P. 2001, *ApJ*, 559, 110
- Zhang, B., & Mészáros, P. 2002, *ApJ*, 566, 712
- Zhang, B. et al. 2006, *ApJ*, 642, 354

Zhang, B. et al. 2007, ApJ, 655, 989

Zhang, B., et al. 2009, ApJ, 703, 1696

Zhang, B., & Pe'er, A. 2009, ApJ, 700, L65

Zhang B., Yan, H., 2011, ApJ, 726, 90

Zou, Y.-C., Fan, Y.-Z., & Piran, T. 2009, MNRAS, 396, 1163

Table 1. The GRBs co-detected by *Fermi* LAT and GBM since *Fermi* science operation and until May, 2010

GRB	z	dur. [sec]	E_p [keV]	$E_{\gamma, \text{iso}}$ [erg]	Fluence ($1 - 10^4$ keV)	Spectral Type	Onset Delay	E_{max}
080825C	-	22	192 ± 15	-	$4.84^{+0.59}_{-0.57} \times 10^{-5}$	BAND	Y	~ 600 MeV
080916C	4.35	66	1443^{+433}_{-303}	$5.7^{+0.54}_{-0.41} \times 10^{54}$	$1.55^{+0.15}_{-0.11} \times 10^{-4}$	BAND	Y	~ 13.2 GeV
081024B	-	0.8	1258^{+2405}_{-522}	-	$(1, 61 \pm 3.8) \times 10^{-6}$	BAND	Y	~ 3 GeV
081215A	-	7.7	1014^{+140}_{-123}	-	$8.74^{+1.21}_{-0.99} \times 10^{-5}$	BAND	-	-
090217	-	32.8	552^{+85}_{-71}	-	$4.48^{+0.69}_{-0.56} \times 10^{-5}$	BAND	N	~ 1 GeV
090323	3.57	150	812^{+181}_{-143}	$> 2.89^{+6.56}_{-0.69} \times 10^{54}$	$> 1.07^{+0.24}_{-0.26} \times 10^{-5}$	BAND	N	~ 1 GeV
090328	0.736	80	756^{+85}_{-72}	$1.02^{+0.087}_{-0.083} \times 10^{53}$	$7.14^{+0.61}_{-0.58} \times 10^{-5}$	BAND	?	> 100 MeV
090510	0.903	0.3	6010^{+2524}_{-1690}	$4.47^{+4.06}_{-3.77} \times 10^{52}$	$2.06^{+1.88}_{-1.74} \times 10^{-5}$	CPL+PL	Y	~ 31 GeV
090626	-	70	362^{+47}_{-41}	-	$7.81^{+0.44}_{-0.38} \times 10^{-5}$	BAND	?	~ 30 GeV
090902B	1.822	21	207 ± 6 [BB]	$(1.77 \pm 0.01) \times 10^{52}$	$(2.10 \pm 0.02) \pm 10^{-4}$	BB+PL	Y	$33.4^{+2.7}_{-3.5}$ GeV
090926A	2.1062	~ 20	412 ± 20	$2.10^{+0.09}_{-0.08} \times 10^{54}$	$1.93^{+0.08}_{-0.07} \times 10^{-4}$	BAND	Y	~ 20 GeV
091003	0.8969	21.1	409^{+34}_{-31}	$7.85^{+0.73}_{-0.57} \times 10^{52}$	$3.68^{+0.34}_{-0.27} \times 10^{-5}$	BAND	N	> 150 MeV
091031	-	~ 40	567^{+197}_{-135}	-	$3.17^{+0.64}_{-0.51} \times 10^{-5}$	BAND	N	1.2 GeV
100116A	-	~ 110	1463^{+163}_{-122}	-	$7.34^{+1.42}_{-1.26} \times 10^{-5}$	BAND	N	~ 2.2 GeV
100225A	-	13 ± 3	540^{+381}_{-204}	-	$1.21^{+1.07}_{-0.57} \times 10^{-5}$	BAND	Y	~ 300 MeV
100325A	-	8.3 ± 1.9	198^{+44}_{-37}	-	$6.15^{+2.85}_{-1.81} \times 10^{-6}$	BAND	N	~ 800 MeV
100414A	1.368	26.4 ± 1.6	520^{+42}_{-39}	$5.88^{+0.69}_{-0.65} \times 10^{53}$	$1.20^{+0.12}_{-0.10} \times 10^{-5}$	BAND	N	~ 2.6 GeV

Note. — References: (1) GRB080825C: z, T_{90} – van der Horst & Connaughton (2008); (2) GRB090916C: z – Greiner et al. (2009), T_{90} – Goldstein & van der Horst (2008), $E_{\gamma, \text{iso}}$ – Abdo et al. (2009a); (3) GRB081024B: T_{90} – Abdo et al. (2010); (4) GRB081215A: T_{90} – Preece (2008); (5) GRB090328: T_{90} – Golenetskii et al. (2009); (6) GRB090510: z – McBreen et al. (2010); (7) GRB090902B: z – Cucchiara et al. (2009a); (8) GRB090926A: z – Malesani et al. (2009); (9) GRB091003: z – Cucchiara et al. (2009b); (10) GRB100414A: z – Cucchiara & Fox (2010)

Table 2. Time-resolved and time-integrated spectral fitting parameters of 17 *Fermi*/LAT GRBs.

080825C Model : Band Function							
Seq	Time s	α	β	E_0 keV	K $\frac{\text{photons}}{\text{keVcm}^2\text{s}} @100\text{keV}$	χ^2	dof
1	0.00-6.75	$-0.57^{+0.05}_{-0.04}$	-2.29 ± 0.04	135^{+10}_{-9}	$0.114^{+0.008}_{-0.007}$	147.1	154
2	6.75-18.1	-0.75 ± 0.06	$-2.35^{+0.09}_{-0.07}$	141^{+16}_{-14}	$0.051^{+0.005}_{-0.004}$	132.7	154
3	18.1-25.0	$-0.95^{+0.17}_{-0.15}$	$-2.17^{+0.17}_{-0.08}$	131^{+56}_{-35}	$0.027^{+0.009}_{-0.006}$	120.1	154
Total	0.00-25.0	-0.73 ± 0.03	$-2.33^{+0.04}_{-0.03}$	148 ± 9	$0.058^{+0.003}_{-0.003}$	265.6	154
080916C Model : Band Function							
Seq	Time s	α	β	E_0 keV	K $\frac{\text{photons}}{\text{keVcm}^2\text{s}} @100\text{keV}$	χ^2	dof
1	0.00-3.70	$-0.69^{+0.05}_{-0.04}$	$-2.49^{+0.13}_{-0.08}$	342^{+43}_{-37}	$0.047^{+0.003}_{-0.002}$	99.5	124
2	3.70-9.10	-1.14 ± 0.03	$-2.32^{+0.06}_{-0.05}$	1680^{+500}_{-348}	0.027 ± 0.001	153.0	124
3	9.10-17.0	$-1.15^{+0.05}_{-0.04}$	$-2.29^{+0.07}_{-0.05}$	975^{+361}_{-235}	0.016 ± 0.001	125.9	124
4	17.0-25.0	-0.99 ± 0.04	$-2.27^{+0.06}_{-0.04}$	447^{+75}_{-60}	0.024 ± 0.001	114.3	124
5	25.0-41.0	-1.08 ± 0.03	$-2.49^{+0.10}_{-0.07}$	666^{+111}_{-87}	0.017 ± 0.001	124.2	124
6	41.0-66.0	-1.09 ± 0.04	$-2.36^{+0.06}_{-0.05}$	696^{+186}_{-128}	0.010 ± 0.001	162.8	124
Total	0.00-66.0	-1.05 ± 0.02	-2.30 ± 0.02	664^{+51}_{-46}	0.018 ± 0.001	427.5	124
081024B Model : Band Function							
Seq	Time s	α	β	E_0 keV	K $\frac{\text{photons}}{\text{keVcm}^2\text{s}} @100\text{keV}$	χ^2	dof
1	-0.300-0.800	$-1.15^{+0.14}_{-0.16}$	$-2.20(\text{fixed})$	1478^{+2810}_{-551}	0.007 ± 0.001	353.9	208
081215A Model : Band Function							
Seq	Time s	α	β	E_0 keV	K $\frac{\text{photons}}{\text{keVcm}^2\text{s}} @100\text{keV}$	χ^2	dof
1	0.00-1.50	-0.65 ± 0.05	$-2.27^{+0.14}_{-0.11}$	753^{+101}_{-88}	0.059 ± 0.002	80.0	71
2	1.50-2.28	$-0.52^{+0.08}_{-0.07}$	$-2.16^{+0.10}_{-0.08}$	280^{+43}_{-39}	$0.223^{+0.020}_{-0.017}$	63.6	61
3	2.28-4.93	-0.60 ± 0.06	$-2.34^{+0.09}_{-0.08}$	178^{+20}_{-17}	$0.156^{+0.013}_{-0.012}$	66.1	77
4	4.93-5.59	$-0.49^{+0.09}_{-0.08}$	$-2.29^{+0.15}_{-0.11}$	214^{+36}_{-31}	$0.266^{+0.032}_{-0.026}$	45.0	54
5	5.59-8.00	$-0.72^{+0.16}_{-0.14}$	$-2.19^{+0.13}_{-0.10}$	102^{+28}_{-22}	$0.093^{+0.029}_{-0.019}$	47.5	82
Total	0.00-8.00	-0.71 ± 0.03	$-2.16^{+0.04}_{-0.03}$	289^{+22}_{-21}	$0.110^{+0.005}_{-0.004}$	179.9	86

Table 2—Continued

090217 Model : Band Function							
Seq	Time s	α	β	E_0 keV	K $\frac{\text{photons}}{\text{keVcm}^2\text{s}}$ @100keV	χ^2	dof
1	0.00-7.50	-0.59 ± 0.04	$-2.56^{+0.10}_{-0.07}$	365^{+33}_{-30}	0.027 ± 0.001	165.1	156
2	7.50-13.1	-0.83 ± 0.05	$-2.66^{+0.37}_{-0.14}$	470^{+20}_{-58}	0.021 ± 0.001	135.5	156
3	13.1-19.7	-0.96 ± 0.09	$-2.38^{+0.22}_{-0.10}$	257^{+73}_{-51}	0.015 ± 0.002	131.1	156
4	19.7-30.0	$-0.52^{+0.43}_{-0.25}$	$-2.22^{+0.17}_{-0.09}$	118^{+65}_{-52}	$0.008^{+0.009}_{-0.003}$	175.4	156
Total	0.00-30.0	-0.81 ± 0.03	$-2.54^{+0.06}_{-0.04}$	418^{+33}_{-30}	0.015 ± 0.001	371.6	156

090323 Model : Band Function							
Seq	Time s	α	β	E_0 keV	K $\frac{\text{photons}}{\text{keVcm}^2\text{s}}$ @100keV	χ^2	dof
1	5.00-14.0	$-0.97^{+0.05}_{-0.04}$	$-2.58^{+0.25}_{-0.13}$	792^{+172}_{-136}	0.016 ± 0.001	98.4	125
2	14.0-25.0	-1.11 ± 0.04	$-2.54^{+0.18}_{-0.10}$	826^{+198}_{-141}	0.017 ± 0.001	127.2	125
3	35.0-50.0	-1.08 ± 0.03	$-2.64^{+0.39}_{-0.15}$	557^{+84}_{-69}	0.018 ± 0.001	151.5	125
4	50.0-60.0	-0.88 ± 0.04	$-2.81^{+1.13}_{-0.24}$	449^{+52}_{-44}	0.026 ± 0.001	115.2	125
5	60.0-135.	$-1.31^{+0.02}_{-0.01}$	$-2.62^{+0.11}_{-0.07}$	987^{+694}_{-116}	0.010 ± 0.001	496.7	125
6	135.-145.	-1.30 ± 0.06	$-2.34^{+0.32}_{-0.12}$	294^{+74}_{-57}	$0.017^{+0.002}_{-0.001}$	208.3	125
Total	0.00-150.	-1.22 ± 0.01	$-2.68^{+0.06}_{-0.04}$	880^{+64}_{-50}	0.012 ± 0.001	857.3	125

090328 Model : Band Function							
Seq	Time s	α	β	E_0 keV	K $\frac{\text{photons}}{\text{keVcm}^2\text{s}}$ @100keV	χ^2	dof
1	3.00-8.00	$-0.92^{+0.04}_{-0.03}$	$-2.38^{+0.16}_{-0.06}$	662^{+99}_{-86}	0.024 ± 0.001	188.0	217
2	12.0-20.0	-0.96 ± 0.02	$-2.38^{+0.09}_{-0.06}$	727^{+80}_{-67}	0.024 ± 0.001	199.3	217
3	20.0-30.0	-1.15 ± 0.03	$-2.30^{+0.09}_{-0.07}$	616^{+81}_{-69}	0.020 ± 0.001	250.7	217
Total	0.00-30.0	-1.05 ± 0.01	$-2.44^{+0.05}_{-0.04}$	791^{+58}_{-50}	0.018 ± 0.001	472.5	217

090510 Model : Cut-off Power-Law+Power Law								
Seq	Time s	Γ_{CPL}	E_0 keV	K_{CPL} $\frac{\text{photons}}{\text{keVcm}^2\text{s}}$ @1keV	Γ_{PL}	K_{PL} $\frac{\text{photons}}{\text{keVcm}^2\text{s}}$ @1keV	χ^2	dof
1	0.450-0.600	-0.76 ± 0.08	2688^{+1360}_{-765}	$1.85^{+0.35}_{-0.63}$	---	---	83.7	230
2	0.600-0.800	$-0.60^{+0.14}_{-0.13}$	4286^{+1760}_{-1130}	$0.47^{+0.53}_{-0.26}$	$-1.73^{+0.06}_{-0.07}$	$23.2^{+13.0}_{-12.3}$	154.9	251
3	0.800-0.900	$-0.75^{+0.67}_{-0.31}$	777^{+1900}_{-464}	$0.97^{+3.41}_{-0.93}$	$-1.60^{+0.11}_{-0.07}$	$14.3^{+17.9}_{-11.6}$	52.0	178
4	0.900-1.00	---	---	---	-1.62 ± 0.06	$11.5^{+7.4}_{-5.8}$	38.0	134
Total	0.450-1.00	$-0.76^{+0.08}_{-0.07}$	3624^{+759}_{-612}	$1.06^{+0.54}_{-0.39}$	$-1.66^{+0.05}_{-0.03}$	$11.9^{+6.2}_{-5.6}$	215.0	272

090626 Model : Band Function							
Seq	Time s	α	β	E_0 keV	K $\frac{\text{photons}}{\text{keVcm}^2\text{s}}$ @100keV	χ^2	dof
1	0.00-9.00	$-0.99^{+0.03}_{-0.02}$	$-2.47^{+0.04}_{-0.03}$	193^{+12}_{-11}	0.079 ± 0.003	340.3	186
2	15.0-20.0	-1.42 ± 0.03	$-2.47^{+0.13}_{-0.08}$	391^{+60}_{-50}	0.040 ± 0.002	155.6	186
3	20.0-27.0	$-1.28^{+0.03}_{-0.02}$	$-2.58^{+0.13}_{-0.08}$	504^{+63}_{-54}	0.034 ± 0.001	136.5	186
4	30.0-40.0	-1.30 ± 0.03	$-2.49^{+0.10}_{-0.06}$	444^{+63}_{-50}	0.025 ± 0.001	211.7	186
Total	0.00-60.0	-1.40 ± 0.01	$-2.62^{+0.04}_{-0.03}$	482^{+27}_{-25}	0.025 ± 0.001	743.3	186

090902B Model : Black Body+Power Law							
Seq	Time s	kT (keV) keV	K_{BB} $\frac{L_{39}}{D_{10}^2}$	Γ_{PL}	K_{PL} $\frac{\text{photons}}{\text{keVcm}^2\text{s}}$ @1keV	χ^2	dof
1	0.00-1.50	$75.60^{+1.86}_{-1.79}$	$38.84^{+1.02}_{-1.03}$	-1.88 ± 0.02	$43.0^{+3.9}_{-3.8}$	330.6	264
2	1.50-2.25	$98.74^{+3.57}_{-3.41}$	$57.13^{+2.25}_{-2.19}$	$-1.84^{+0.03}_{-0.04}$	$31.1^{+5.3}_{-4.3}$	226.3	237
3	2.25-2.81	$121.20^{+5.00}_{-4.79}$	$84.54^{+3.79}_{-3.72}$	$-1.81^{+0.03}_{-0.04}$	$27.5^{+4.6}_{-4.3}$	217.5	238
4	2.81-3.23	$82.52^{+4.32}_{-3.97}$	$58.00^{+3.05}_{-2.88}$	$-1.80^{+0.03}_{-0.04}$	$33.6^{+6.4}_{-5.3}$	199.0	217
5	3.23-3.83	$100.90^{+3.76}_{-3.57}$	$69.22^{+2.81}_{-2.71}$	$-1.83^{+0.03}_{-0.04}$	$34.7^{+6.0}_{-4.8}$	190.7	240
6	3.83-4.46	$86.81^{+2.92}_{-2.79}$	$60.01^{+2.20}_{-2.14}$	$-1.83^{+0.03}_{-0.04}$	$33.4^{+5.7}_{-4.7}$	218.3	236
7	4.46-4.99	$90.79^{+4.78}_{-4.43}$	$47.82^{+2.65}_{-2.52}$	$-1.83^{+0.03}_{-0.04}$	$38.6^{+6.4}_{-5.2}$	207.4	225
8	4.99-5.45	$109.50^{+4.32}_{-4.11}$	$88.50^{+3.82}_{-3.68}$	$-1.82^{+0.04}_{-0.05}$	$31.5^{+6.6}_{-5.2}$	185.3	228
9	5.45-5.86	$116.20^{+5.20}_{-4.94}$	$85.70^{+4.22}_{-4.13}$	$-1.82^{+0.04}_{-0.05}$	$34.6^{+7.2}_{-5.9}$	180.5	227
10	5.86-6.28	$132.60^{+4.36}_{-4.21}$	$141.20^{+5.27}_{-5.14}$	$-1.81^{+0.04}_{-0.05}$	$32.5^{+6.5}_{-5.3}$	186.5	233
11	6.28-6.61	$157.40^{+6.74}_{-6.50}$	$155.60^{+7.77}_{-7.36}$	$-1.81^{+0.04}_{-0.06}$	$38.0^{+8.6}_{-6.0}$	186.2	228
12	6.61-7.19	$171.10^{+5.01}_{-4.85}$	$174.10^{+5.97}_{-5.80}$	$-1.86^{+0.02}_{-0.03}$	$87.2^{+8.6}_{-7.3}$	229.0	248
13	7.19-7.65	$174.20^{+5.55}_{-5.35}$	$207.90^{+7.57}_{-7.37}$	$-1.87^{+0.02}_{-0.03}$	$124.3^{+12.1}_{-10.3}$	231.3	244
14	7.65-8.00	$217.80^{+7.47}_{-7.29}$	$307.00^{+13.50}_{-12.20}$	-1.87 ± 0.02	$203.5^{+13.0}_{-13.2}$	223.0	243

Table 2—Continued

15	8.00-8.50	204.80 ^{+5.62} _{-5.48}	288.60 ^{+9.22} _{-9.01}	-1.91 ± 0.01	344.6 ^{+17.3} _{-15.7}	319.9	248
16	8.50-9.00	206.60 ^{+5.97} _{-5.83}	281.00 ^{+9.35} _{-9.16}	-1.93 ^{+0.01} _{-0.02}	375.7 ^{+21.5} _{-19.3}	260.2	249
17	9.00-9.50	206.20 ^{+5.99} _{-5.83}	270.50 ^{+9.11} _{-8.91}	-1.92 ± 0.01	445.6 ^{+20.5} _{-18.9}	325.6	248
18	9.50-10.0	135.90 ^{+3.26} _{-3.18}	209.90 ^{+5.53} _{-5.45}	-1.96 ^{+0.01} _{-0.02}	553.2 ^{+28.6} _{-26.0}	271.2	244
19	10.0-10.5	168.80 ^{+4.58} _{-4.47}	236.40 ^{+7.18} _{-7.04}	-1.94 ± 0.02	378.4 ^{+23.8} _{-20.9}	258.3	244
20	10.5-11.0	195.70 ^{+6.03} _{-5.89}	246.60 ^{+8.70} _{-8.50}	-1.90 ± 0.01	352.5 ^{+17.7} _{-16.0}	348.6	247
21	11.0-11.5	145.20 ^{+4.50} _{-4.34}	179.10 ^{+5.98} _{-5.81}	-1.93 ± 0.02	332.2 ^{+20.8} _{-18.3}	278.5	242
22	11.5-12.0	153.10 ^{+4.43} _{-4.32}	169.30 ^{+5.68} _{-5.56}	-1.92 ± 0.02	253.5 ^{+18.8} _{-16.2}	241.9	241
23	12.0-12.4	61.07 ^{+3.09} _{-2.90}	44.61 ^{+2.31} _{-2.22}	-1.90 ± 0.02	242.6 ^{+18.4} _{-15.8}	194.7	214
24	12.4-13.2	35.36 ^{+0.92} _{-0.88}	31.80 ^{+0.94} _{-0.90}	-1.92 ± 0.01	271.2 ^{+15.8} _{-11.9}	324.6	231
25	13.2-13.3	42.30 ^{+1.68} _{-1.59}	87.55 ^{+3.92} _{-3.83}	-1.84 ± 0.03	213.7 ^{+27.0} _{-22.7}	141.4	180
26	13.3-13.6	45.32 ^{+2.10} _{-1.97}	57.60 ^{+2.72} _{-2.79}	-1.87 ± 0.02	276.6 ^{+23.4} _{-20.6}	175.3	192
27	13.6-13.8	53.27 ^{+2.02} _{-1.94}	69.62 ^{+2.90} _{-2.85}	-1.87 ^{+0.02} _{-0.03}	203.7 ^{+20.6} _{-17.3}	169.2	199
28	13.8-14.1	66.19 ^{+2.92} _{-2.79}	89.79 ^{+3.93} _{-3.80}	-1.84 ± 0.02	187.8 ^{+15.3} _{-13.8}	275.3	206
29	14.1-14.2	105.70 ^{+5.22} _{-4.91}	201.80 ^{+10.2} _{-9.99}	-1.82 ± 0.03	169.6 ^{+20.2} _{-18.2}	177.9	204
30	14.2-14.4	120.40 ^{+5.93} _{-5.70}	199.60 ^{+10.40} _{-10.00}	-1.83 ^{+0.02} _{-0.03}	159.9 ^{+18.7} _{-15.2}	180.7	211
31	14.4-14.6	51.74 ^{+2.45} _{-2.30}	57.16 ^{+2.86} _{-2.79}	-1.86 ^{+0.02} _{-0.03}	186.8 ^{+15.8} _{-16.2}	164.6	194
32	14.6-14.8	99.11 ^{+4.23} _{-4.00}	155.80 ^{+6.88} _{-6.57}	-1.85 ± 0.03	160.5 ^{+19.3} _{-15.4}	173.6	211
33	14.8-15.0	71.48 ^{+3.30} _{-3.09}	115.90 ^{+5.55} _{-5.38}	-1.82 ± 0.03	149.0 ^{+19.0} _{-15.9}	165.7	196
34	15.0-15.1	102.20 ^{+5.60} _{-5.26}	220.80 ^{+12.2} _{-11.7}	-1.81 ± 0.03	159.0 ^{+21.9} _{-18.3}	184.4	202
35	15.1-15.2	102.10 ^{+4.40} _{-4.22}	233.10 ^{+10.5} _{-10.1}	-1.81 ± 0.03	144.6 ^{+18.9} _{-15.4}	212.1	199
36	15.2-15.5	127.0 ^{+3.85} _{-3.73}	223.0 ^{+7.36} _{-7.18}	-1.85 ^{+0.0201} _{-0.0234}	160.7 ^{+14.3} _{-12.5}	216.60	215
37	15.5-15.7	150.70 ^{+6.16} _{-5.99}	254.80 ^{+11.80} _{-11.30}	-1.83 ± 0.03	120.5 ^{+15.9} _{-12.4}	168.4	221
38	15.7-16.2	59.42 ^{+1.81} _{-1.74}	63.99 ^{+2.15} _{-2.12}	-1.88 ± 0.02	169.4 ^{+14.3} _{-12.4}	197.2	221
39	16.2-16.3	84.53 ^{+3.95} _{-3.69}	132.10 ^{+6.36} _{-6.08}	-1.84 ± 0.03	168.9 ^{+20.3} _{-16.5}	190.3	203
40	16.3-16.5	90.82 ^{+3.67} _{-3.47}	160.90 ^{+6.85} _{-6.63}	-1.83 ± 0.03	158.1 ^{+18.3} _{-15.4}	177.3	206
41	16.5-16.7	94.44 ^{+4.55} _{-4.25}	143.00 ^{+7.11} _{-6.81}	-1.84 ± 0.03	160.6 ^{+19.1} _{-15.8}	169.6	210
42	16.7-16.9	78.69 ^{+4.46} _{-4.10}	96.94 ^{+5.55} _{-5.29}	-1.83 ^{+0.03} _{-0.04}	137.2 ^{+18.4} _{-15.4}	155.4	198
43	16.9-17.1	47.97 ^{+2.65} _{-2.47}	40.30 ^{+2.33} _{-2.26}	-1.84 ^{+0.02} _{-0.03}	138.7 ^{+19.3} _{-13.1}	144.2	191
44	17.1-17.5	63.52 ^{+2.29} _{-2.19}	75.35 ^{+2.93} _{-2.87}	-1.86 ^{+0.02} _{-0.03}	148.8 ^{+15.6} _{-13.1}	171.4	206
45	17.5-17.8	68.97 ^{+3.46} _{-3.26}	54.62 ^{+2.85} _{-2.76}	-1.85 ^{+0.02} _{-0.03}	113.7 ^{+12.6} _{-10.6}	191.9	209
46	17.8-18.3	46.21 ^{+1.56} _{-1.50}	38.75 ^{+1.39} _{-1.36}	-1.87 ± 0.02	142.8 ^{+10.4} _{-9.5}	248.0	228
47	18.3-18.9	57.27 ^{+1.95} _{-1.85}	52.36 ^{+1.80} _{-1.75}	-1.88 ± 0.02	166.4 ^{+10.6} _{-9.8}	334.0	233
48	18.9-19.4	57.29 ^{+1.97} _{-1.87}	49.10 ^{+1.75} _{-1.71}	-1.88 ± 0.02	156.0 ^{+10.7} _{-9.7}	302.1	220
49	19.4-19.6	49.44 ^{+1.96} _{-1.86}	81.63 ^{+3.50} _{-3.39}	-1.83 ± 0.03	147.1 ^{+18.8} _{-15.7}	167.7	189
50	19.6-19.7	54.68 ^{+2.24} _{-2.14}	88.95 ^{+3.88} _{-3.81}	-1.83 ^{+0.02} _{-0.03}	164.9 ^{+18.9} _{-16.3}	171.8	192
51	19.7-19.9	57.57 ^{+2.54} _{-2.43}	94.89 ^{+4.29} _{-4.21}	-1.83 ^{+0.02} _{-0.03}	178.0 ^{+18.0} _{-16.0}	202.2	194
52	19.9-20.1	72.81 ^{+1.16} _{-1.16}	91.88 ^{+2.28} _{-2.28}	-1.85 ^{+0.02} _{-0.03}	197.8 ^{+20.5} _{-17.5}	170.6	196
53	20.1-20.3	43.33 ^{+3.37} _{-3.07}	42.35 ^{+2.99} _{-2.88}	-1.82 ^{+0.02} _{-0.03}	136.6 ^{+16.6} _{-14.9}	165.1	189
54	20.3-20.6	50.94 ^{+2.52} _{-2.41}	53.85 ^{+2.64} _{-2.59}	-1.86 ± 0.02	193.9 ^{+17.2} _{-15.3}	221.4	205
55	20.6-20.9	46.04 ^{+1.79} _{-1.71}	51.23 ^{+2.16} _{-2.12}	-1.87 ± 0.02	192.5 ^{+16.7} _{-14.8}	192.6	196
56	20.9-21.0	42.49 ^{+2.20} _{-2.04}	55.46 ^{+2.90} _{-2.79}	-1.84 ± 0.03	148.9 ^{+18.6} _{-16.0}	171.3	183
57	21.0-21.3	36.47 ^{+2.44} _{-2.20}	23.88 ^{+1.59} _{-1.53}	-1.87 ^{+0.02} _{-0.03}	152.9 ^{+17.0} _{-14.5}	143.5	189
58	21.3-21.7	42.84 ^{+1.23} _{-1.19}	50.72 ^{+1.67} _{-1.63}	-1.88 ^{+0.02} _{-0.03}	155.2 ^{+14.8} _{-12.7}	186.5	212
59	21.7-21.9	47.05 ^{+2.89} _{-2.70}	46.19 ^{+2.80} _{-2.80}	-1.84 ^{+0.02} _{-0.03}	161.9 ^{+17.8} _{-15.5}	152.6	195
60	21.9-22.2	49.53 ^{+3.39} _{-3.13}	42.03 ^{+2.94} _{-2.83}	-1.84 ^{+0.02} _{-0.03}	153.6 ^{+17.5} _{-15.1}	147.1	188
61	22.2-23.0	31.13 ^{+4.08} _{-3.30}	5.72 ^{+0.62} _{-0.60}	-1.90 ± 0.02	126.0 ^{+10.2} _{-9.4}	187.3	233
Total	0.00-30.0	96.71 ^{+0.461} _{-0.484}	71.65 ^{+0.34} _{-0.36}	-1.93 ± 0.01	175.1 ^{+1.2} _{-1.3}	14732.0	276

090902B Model : Band Function + Power Law

	Time s	α	β	E_0 keV	K $\frac{\text{photons}}{\text{keVcm}^2\text{s}} @100\text{keV}$	Γ_{PL}	K_{PL} $\frac{\text{photons}}{\text{keVcm}^2\text{s}} @1\text{keV}$	χ^2	dof
Total	0.00-23.0	-0.83 ± 0.01	-3.68 ^{+0.12} _{-0.20}	724 ⁺¹³ ₋₁₂	0.099 ± 0.001	-1.85 ^{+1.85} _{-1.85}	43.4 ± 1.5	2024.3	275

090926A Model : Band Function

Seq	Time s	α	β	E_0 keV	K $\frac{\text{photons}}{\text{keVcm}^2\text{s}} @100\text{keV}$	χ^2	dof
1	0.00-2.81	-0.53 ^{+0.04} _{-0.03}	-2.43 ^{+0.06} _{-0.05}	235 ⁺¹⁶ ₋₁₅	0.106 ± 0.004	189.0	210
2	2.81-3.75	-0.48 ± 0.03	-2.75 ^{+0.21} _{-0.13}	255 ⁺¹⁵ ₋₁₄	0.303 ^{+0.011} _{-0.010}	168.6	196
3	3.75-5.62	-0.57 ± 0.02	-2.35 ± 0.02	208 ± 8	0.344 ± 0.009	269.1	213
4	5.62-7.50	-0.73 ± 0.02	-2.50 ^{+0.13} _{-0.08}	326 ± 15	0.191 ± 0.004	229.7	210
5	7.50-9.38	-0.63 ± 0.03	-2.81 ^{+0.17} _{-0.13}	183 ⁺⁹ ₋₈	0.255 ^{+0.009} _{-0.008}	169.6	209
6	9.38-11.2	-0.75 ± 0.02	-2.52 ^{+0.10} _{-0.08}	193 ⁺⁹ ₋₈	0.327 ^{+0.010} _{-0.009}	228.1	213
7	11.2-13.1	-0.80 ± 0.03	-2.29 ^{+0.06} _{-0.05}	154 ⁺¹¹ ₋₁₀	0.242 ^{+0.012} _{-0.012}	186.1	212
8	13.1-15.9	-0.99 ± 0.05	-2.36 ^{+0.22} _{-0.11}	161 ⁺²² ₋₁₉	0.081 ^{+0.008} _{-0.007}	164.7	213
9	15.9-20.0	-1.26 ± 0.08	-2.07 ^{+0.07} _{-0.04}	216 ⁺⁶⁸ ₋₄₈	0.025 ^{+0.004} _{-0.003}	170.9	214
Total	0.00-20.0	-0.74 ± 0.01	-2.34 ± 0.01	226 ± 4	0.165 ± 0.002	777.1	216

091003 Model : Band Function

Table 2—Continued

Seq	Time s	α	β	E_0 keV	K $\frac{\text{photons}}{\text{keV cm}^2 \text{s}} @ 100 \text{keV}$	χ^2	dof
1	7.00-15.0	-1.33 ± 0.05	$-2.41^{+0.20}_{-0.10}$	426^{+101}_{-77}	0.012 ± 0.001	234.5	246
2	15.0-18.0	-1.01 ± 0.04	$-2.52^{+0.19}_{-0.10}$	337^{+43}_{-38}	0.040 ± 0.002	152.4	243
3	18.0-20.0	-0.85 ± 0.03	$-2.55^{+0.10}_{-0.07}$	357^{+28}_{-26}	0.094 ± 0.003	218.9	242
4	20.0-26.0	$-1.36^{+0.06}_{-0.05}$	$-2.35^{+0.15}_{-0.08}$	429^{+143}_{-97}	0.014 ± 0.001	189.2	246
Total	0.00-26.0	$-1.09^{+0.02}_{-0.01}$	$-2.58^{+0.05}_{-0.04}$	474^{+27}_{-25}	0.024 ± 0.001	446.2	246
091031 Model : Band Function							
Seq	Time s	α	β	E_0 keV	K $\frac{\text{photons}}{\text{keV cm}^2 \text{s}} @ 100 \text{keV}$	χ^2	dof
1	0.00-8.00	-0.89 ± 0.06	$-2.44^{+0.09}_{-0.07}$	496^{+111}_{-84}	0.013 ± 0.001	177.1	186
2	8.00-15.0	$-0.86^{+0.06}_{-0.05}$	$-2.50^{+0.13}_{-0.08}$	357^{+55}_{-47}	0.020 ± 0.001	173.3	186
3	15.0-25.0	$-0.78^{+0.11}_{-0.10}$	$-2.55^{+0.26}_{-0.12}$	467^{+157}_{-104}	0.006 ± 0.001	187.1	186
Total	0.00-25.0	$-0.87^{+0.04}_{-0.03}$	$-2.55^{+0.06}_{-0.05}$	458^{+51}_{-33}	0.012 ± 0.001	347.2	186
100116A Model : Band Function							
Seq	Time s	α	β	E_0 keV	K $\frac{\text{photons}}{\text{keV cm}^2 \text{s}} @ 100 \text{keV}$	χ^2	dof
1	-2.00-5.00	$-1.03^{+0.13}_{-0.11}$	$-2.54^{+2.54}_{-0.24}$	384^{+201}_{-124}	0.006 ± 0.001	104.8	155
2	80.0-90.0	$-1.03^{+0.05}_{-0.04}$	$-2.80^{+0.97}_{-0.21}$	791^{+192}_{-142}	0.010 ± 0.001	127.8	155
3	90.0-95.0	-1.00 ± 0.01	$-3.22^{+1.51}_{-0.25}$	1459^{+161}_{-121}	0.033 ± 0.001	156.9	155
4	95.0-110.	-1.03 ± 0.05	$-2.63^{+0.23}_{-0.11}$	677^{+169}_{-120}	0.009 ± 0.001	127.0	155
Total	0.00-110.	$-1.11^{+0.01}_{-0.02}$	$-3.13^{+0.11}_{-0.09}$	2867^{+430}_{-283}	0.004 ± 0.001	415.6	155
100225A Model : Band Function							
Seq	Time s	α	β	E_0 keV	K $\frac{\text{photons}}{\text{keV cm}^2 \text{s}} @ 100 \text{keV}$	χ^2	dof
1	0.00-6.00	$-0.53^{+0.22}_{-0.19}$	$-2.43^{+0.87}_{-0.19}$	263^{+120}_{-74}	0.010 ± 0.002	51.8	94
2	6.00-12.0	$-0.93^{+0.15}_{-0.13}$	$-2.30^{+0.26}_{-0.12}$	507^{+351}_{-181}	$0.009^{+0.002}_{-0.001}$	40.3	93
Total	0.00-12.0	$-0.77^{+0.12}_{-0.11}$	$-2.37^{+0.18}_{-0.10}$	375^{+129}_{-86}	0.010 ± 0.001	64.5	94
100325A Model : Band Function							
Seq	Time s	α	β	E_0 keV	K $\frac{\text{photons}}{\text{keV cm}^2 \text{s}} @ 100 \text{keV}$	χ^2	dof
1	-3.00-10.0	$-0.72^{+0.11}_{-0.10}$	$-2.60^{+1.89}_{-0.21}$	155^{+32}_{-26}	0.014 ± 0.002	151.6	125
100414A Model : Band Function							
Seq	Time s	α	β	E_0 keV	K $\frac{\text{photons}}{\text{keV cm}^2 \text{s}} @ 100 \text{keV}$	χ^2	dof
1	1.00-7.25	$-0.19^{+0.06}_{-0.05}$	$-2.54^{+0.16}_{-0.10}$	256^{+22}_{-20}	0.036 ± 0.002	124.3	156
2	7.25-14.3	$-0.25^{+0.05}_{-0.04}$	$-2.89^{+0.51}_{-0.24}$	281^{+19}_{-20}	$0.040^{+0.002}_{-0.001}$	124.5	156
3	14.3-19.6	$-0.56^{+0.04}_{-0.03}$	$-2.53^{+0.16}_{-0.10}$	361^{+28}_{-26}	0.047 ± 0.002	135.1	156
4	19.6-25.5	-0.76 ± 0.03	$-2.45^{+0.11}_{-0.07}$	386^{+30}_{-28}	0.052 ± 0.002	131.9	156
Total	1.00-26.0	-0.52 ± 0.02	$-2.62^{+0.07}_{-0.05}$	344^{+12}_{-12}	0.042 ± 0.001	281.7	156

Note. — Spectral models used in this paper, i.e, Band Function (BAND), Black-Body (BB), Cut-off Power Law (CPL), and Power-Law (PL), correspond to grbm, bbody, cutoffpl and powerlaw in XSPEC package, respectively. Details of the formulae of these models can be found at <http://heasarc.gsfc.nasa.gov/docs/xanadu/xspec/manual/XspecModels.html>.

Table 3. Temporal decay slopes and the time integrated photon indices of the long-term LAT count rate lightcurves

Name	α_{LAT}	$\bar{\Gamma}_{\text{LAT}}$
080825C	-0.47 ± 0.74	-1.71
080916C	-1.33 ± 0.08	-1.77
081024B	-1.37 ± 0.41	-1.98
081215A	-	-
090217	-0.81 ± 0.23	-1.97
090323	-0.52 ± 0.67	-1.75
090328	-0.96 ± 0.44	-1.82
090510	-1.70 ± 0.08	-1.94
090626	-	-1.53
090902B	-1.40 ± 0.06	-1.76
090926A	-2.05 ± 0.14	-2.03
091003	< -0.93	-1.74
091031	-0.57 ± 0.28	-1.73
100116A	-	-1.68
100225A	-	-1.77
100325A	< -1.04	-1.53
100414A	-1.64 ± 0.89	-1.85

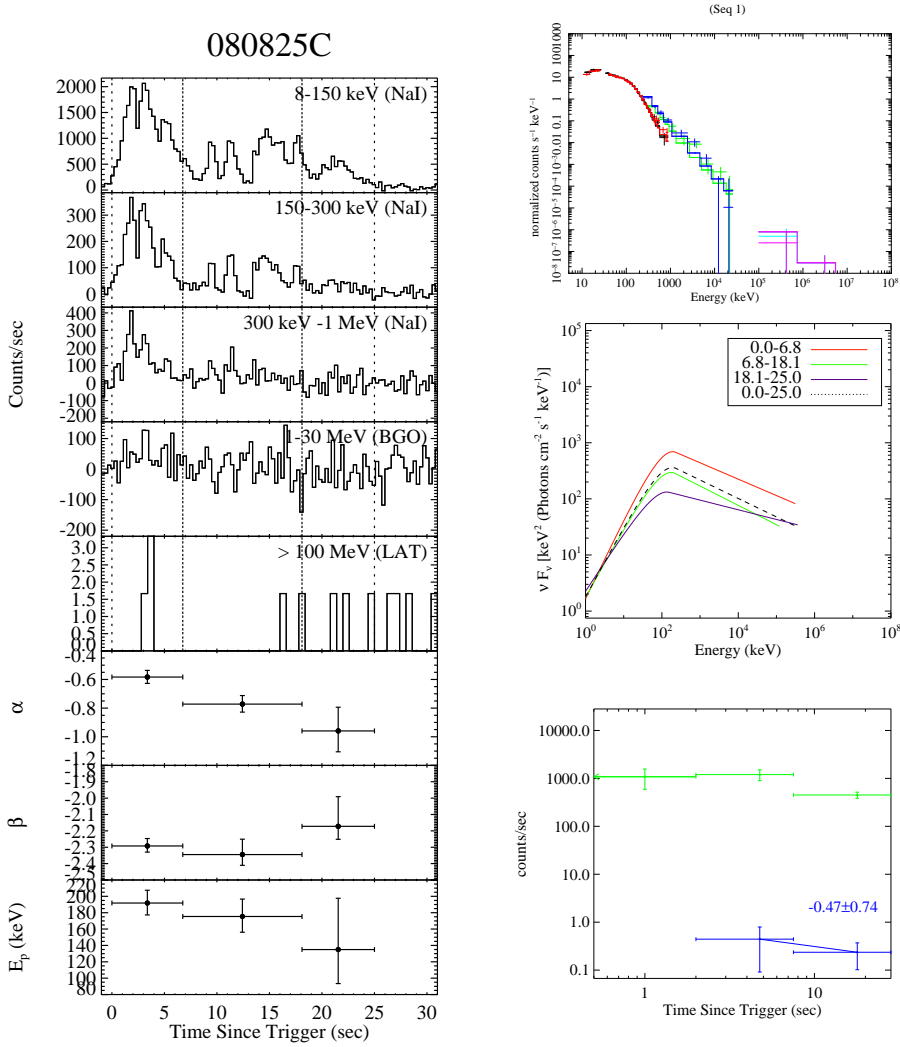


Fig. 1.— Joint temporal and spectral analysis of GBM and LAT data for GRB 080825C. *Left panels:* the background-subtracted GBM and LAT lightcurves (from top: 8-150 keV, 150-300 keV, 300 keV - 1 MeV, 1-30 MeV, >100 MeV), and evolution of spectra parameters (α , β , E_p). *Right panels:* an example (the brightest episode) of the observed photon spectrum as compared with the spectral model (*top*), the best fit νF_ν spectra of all time bins (*middle*), and the comparison between the GBM (green) and LAT (blue) count rate lightcurves in log-scale (*bottom*).

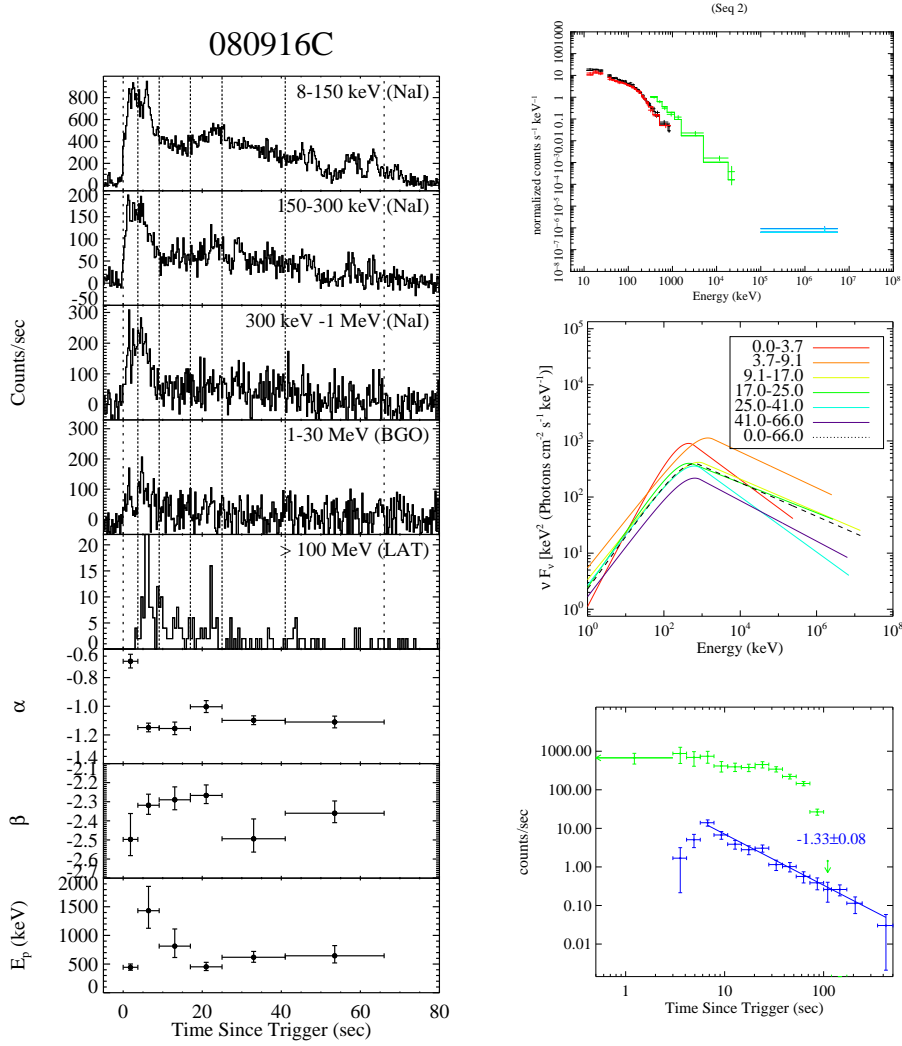


Fig. 2.— Same as Figure 1, but for GRB 080916C.

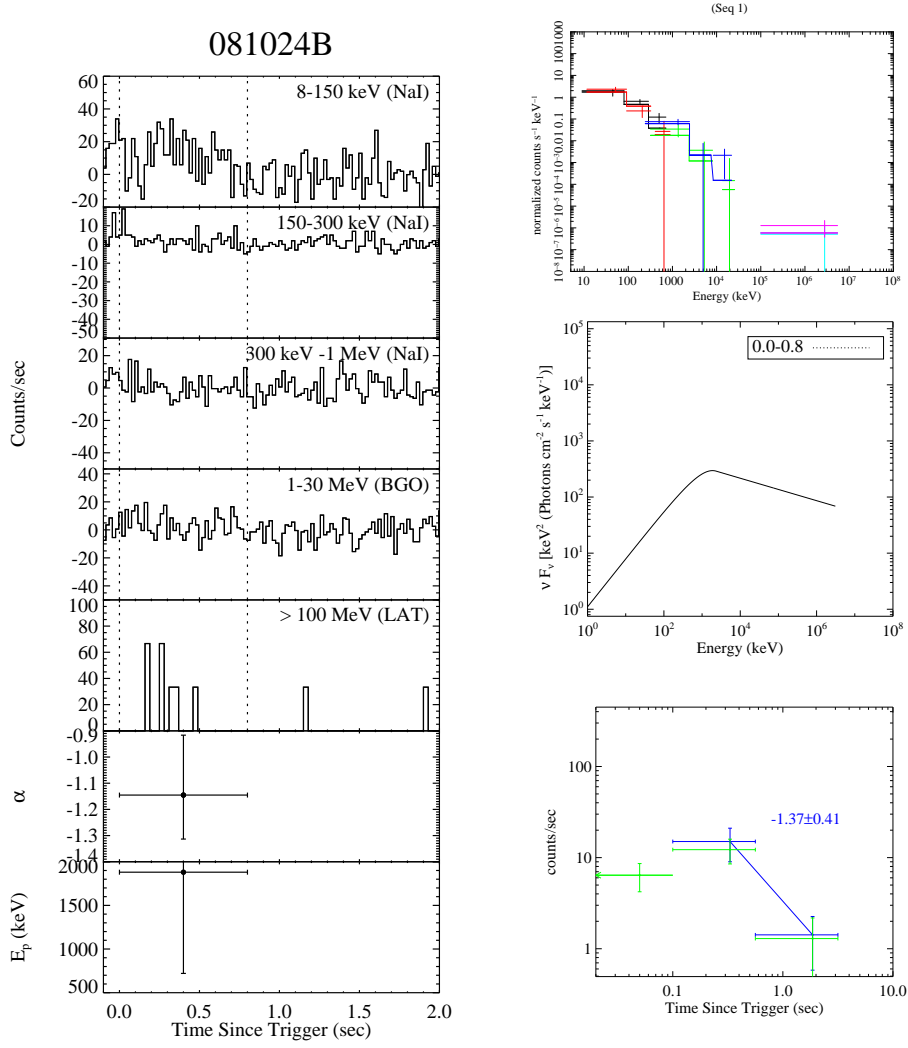


Fig. 3.— Same as Figure 1, but for GRB 081024B.

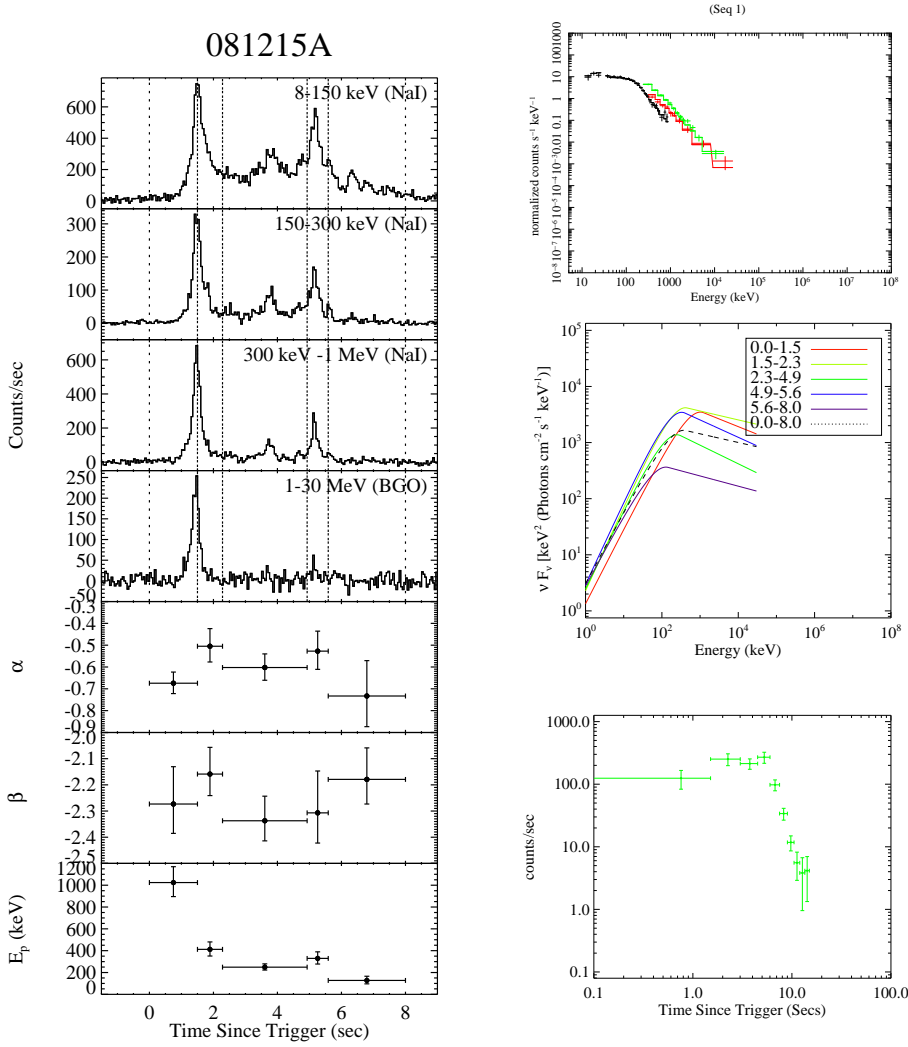


Fig. 4.— Same as Figure 1, but for GRB 081215A. This burst was at an angle of 86 degrees to the LAT boresight. The data cannot be obtained with the standard analysis procedures. Using a non-standard data selection, over 100 counts above background were detected within a 0.5 s interval in coincidence with the main GBM peak (McEnery et al. 2008). We thus add this GRB in our sample, but do not add its LAT data in our analysis.

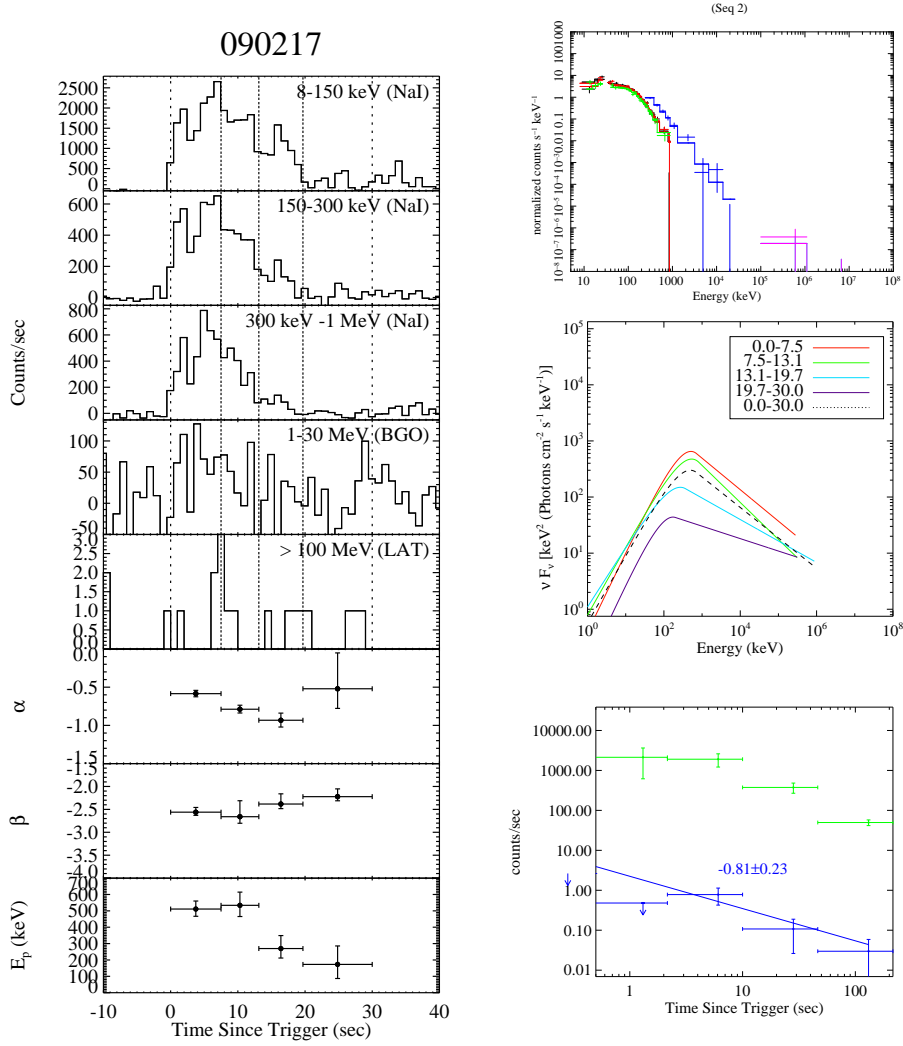


Fig. 5.— Same as Figure 1, but for GRB 090217.

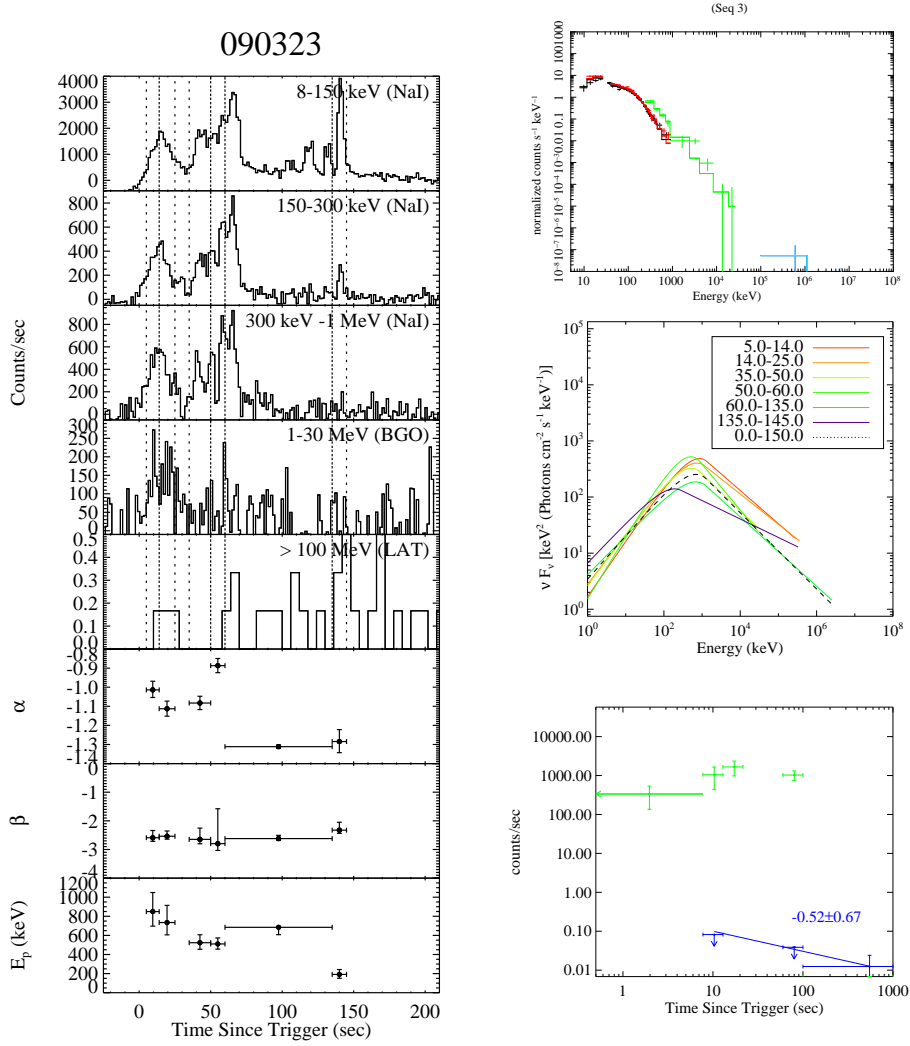


Fig. 6.— Same as Figure 1, but for GRB 090323.

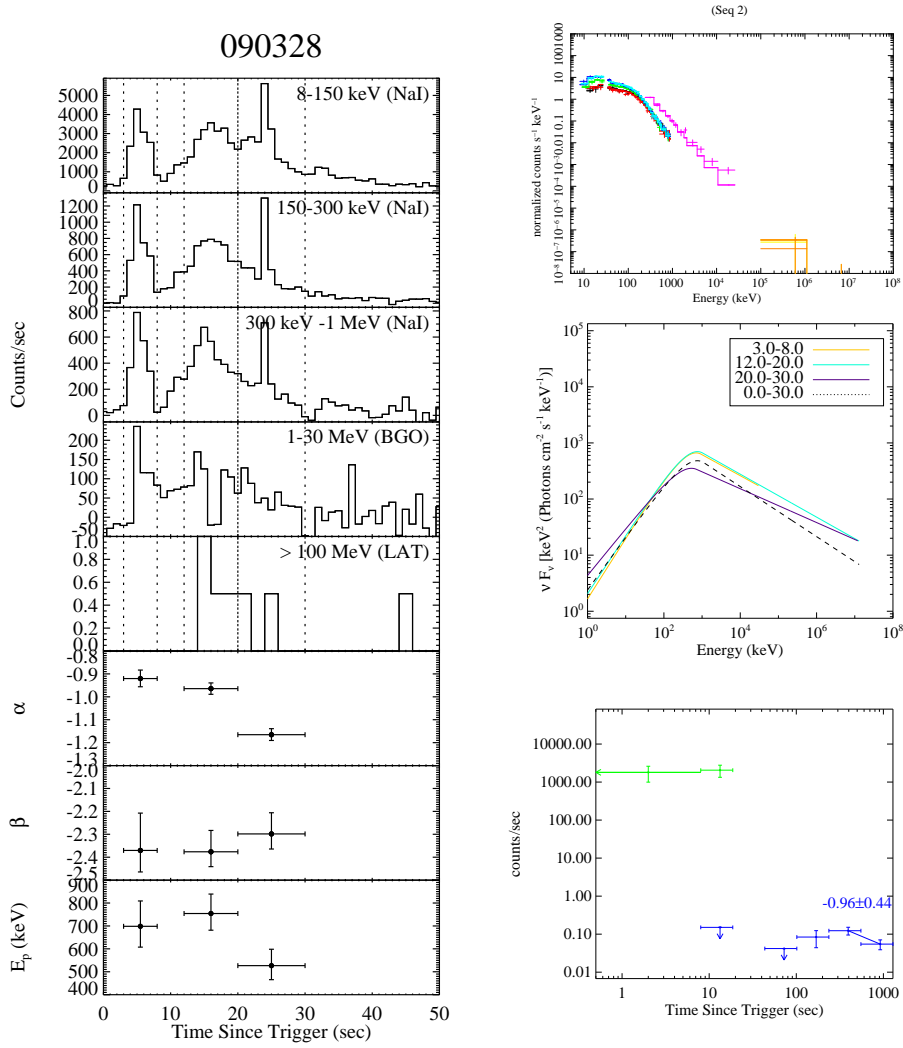


Fig. 7.— Same as Figure 1, but for GRB 090328.

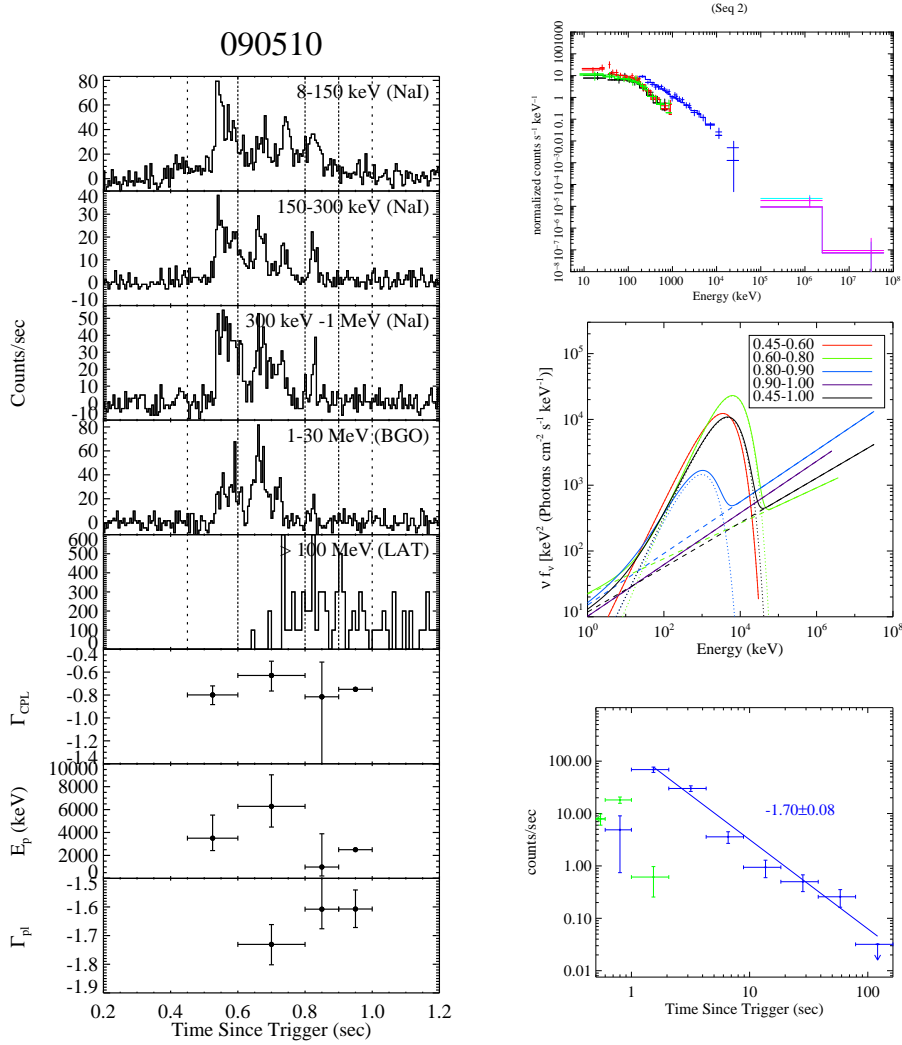


Fig. 8.— Same as Figure 1, but for GRB 090510. The applied model is cut-off power-law plus power-law (CPL + PL).

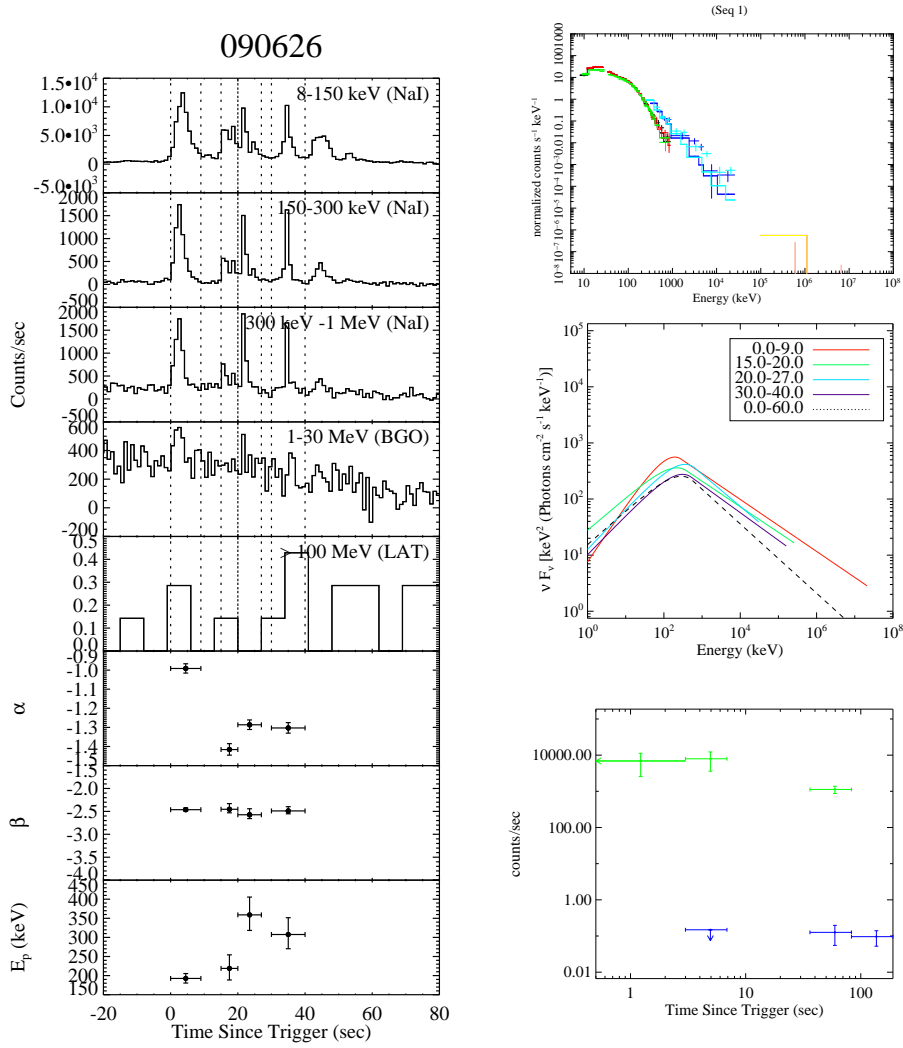


Fig. 9.— Same as Figure 1, but for GRB 090626.

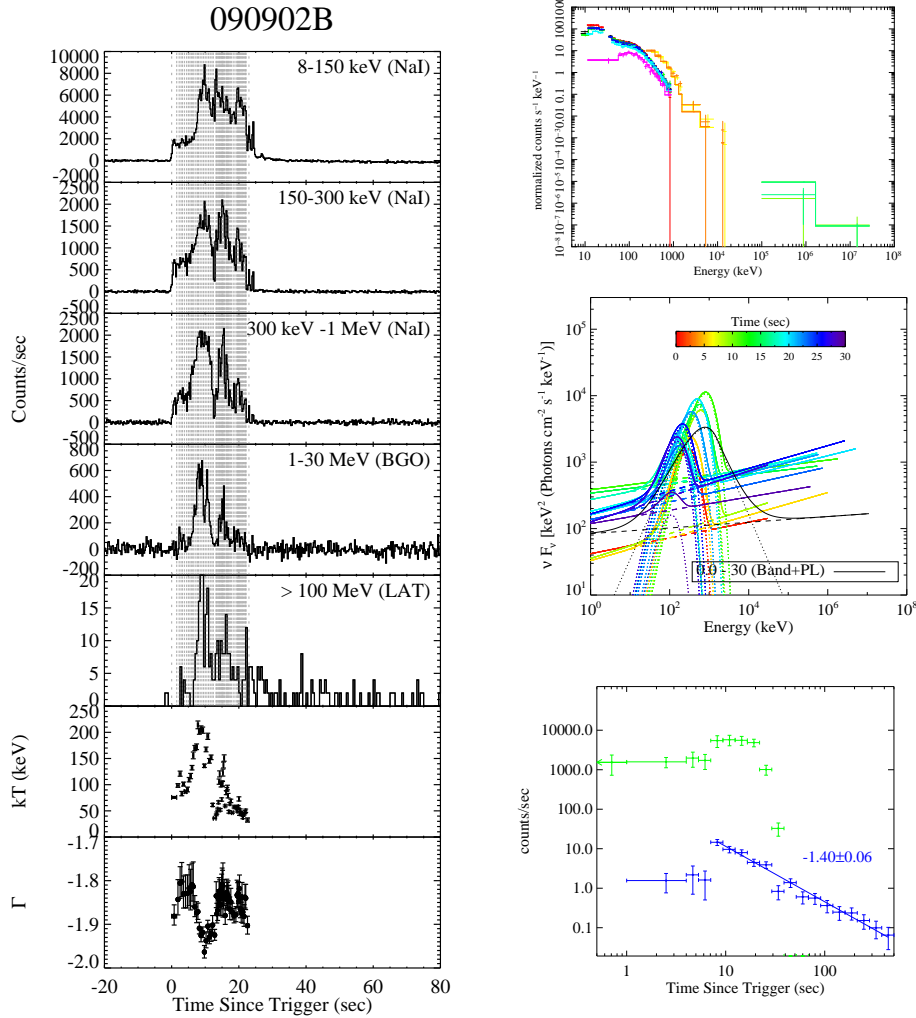


Fig. 10.— Same as Fig. 1, but for GRB 090902B. The applied model is blackbody plus power law (BB + PL).

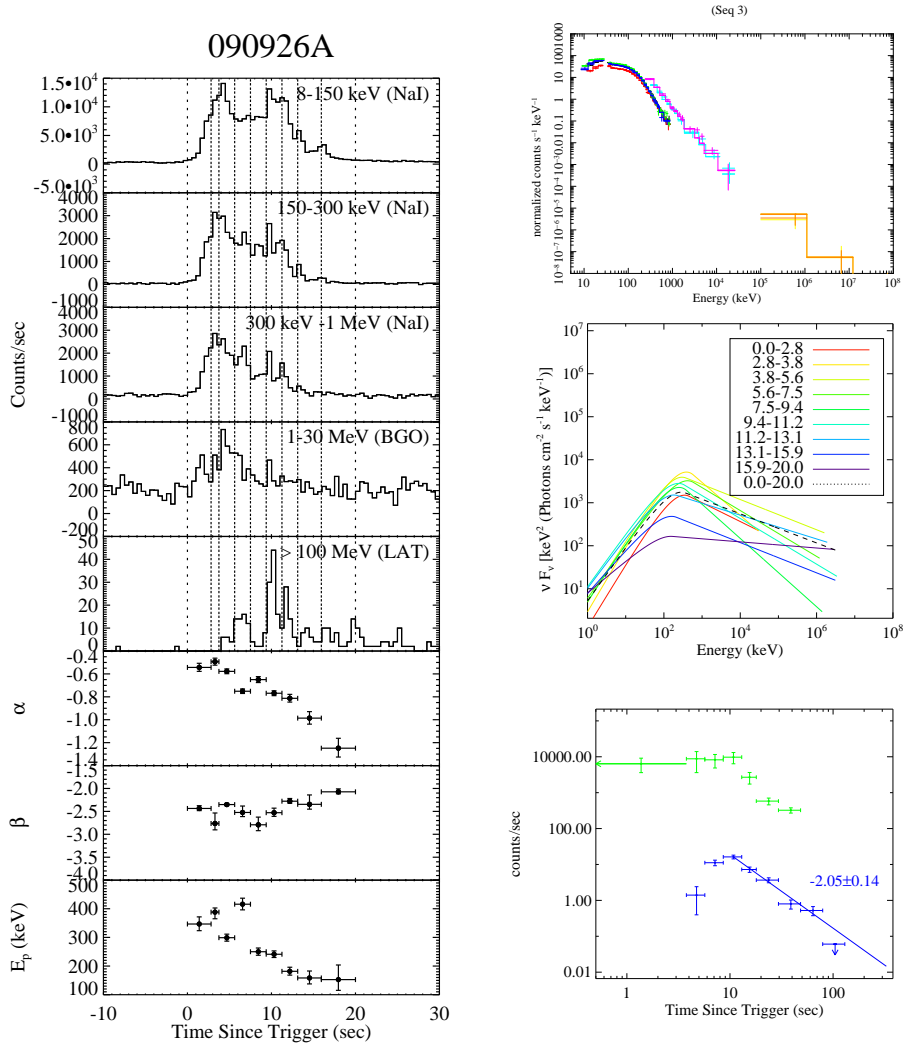


Fig. 11.— Same as Figure 1, but for GRB 090926A.

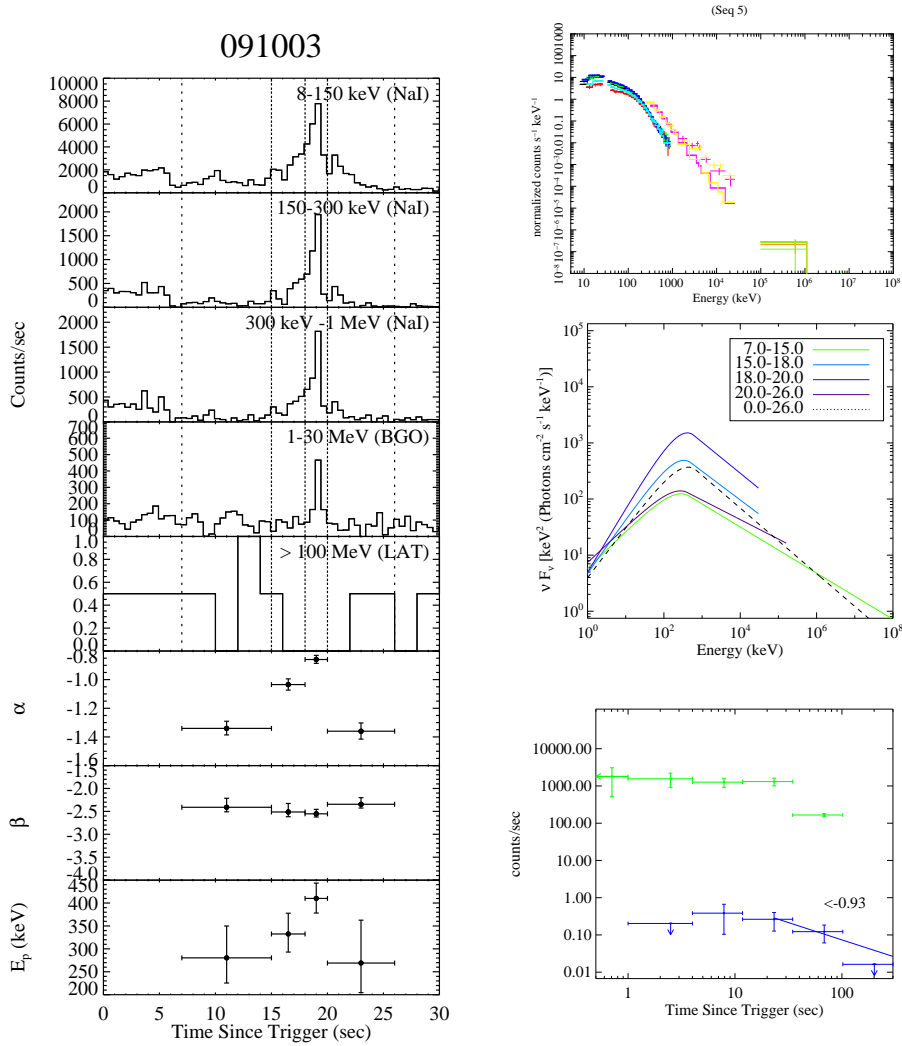


Fig. 12.— Same as Figure 1, but for GRB 091003.

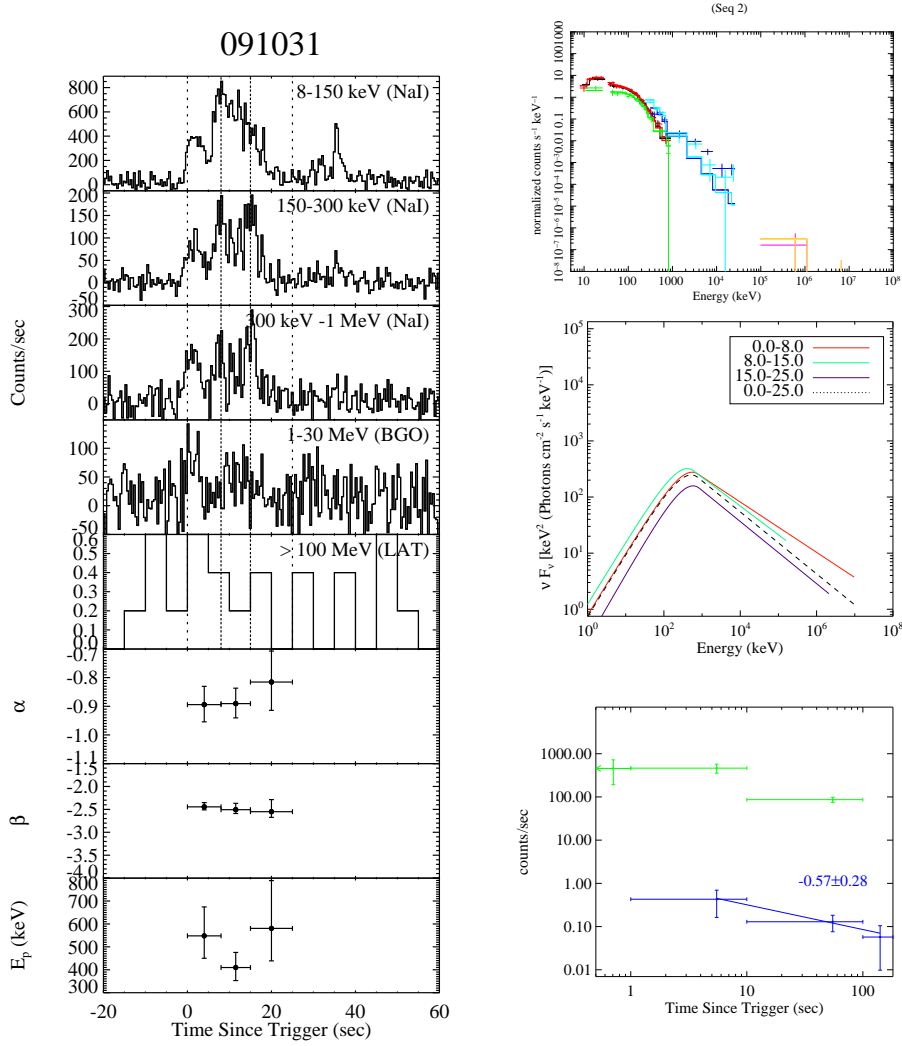


Fig. 13.— Same as Figure 1, but for GRB 091031.

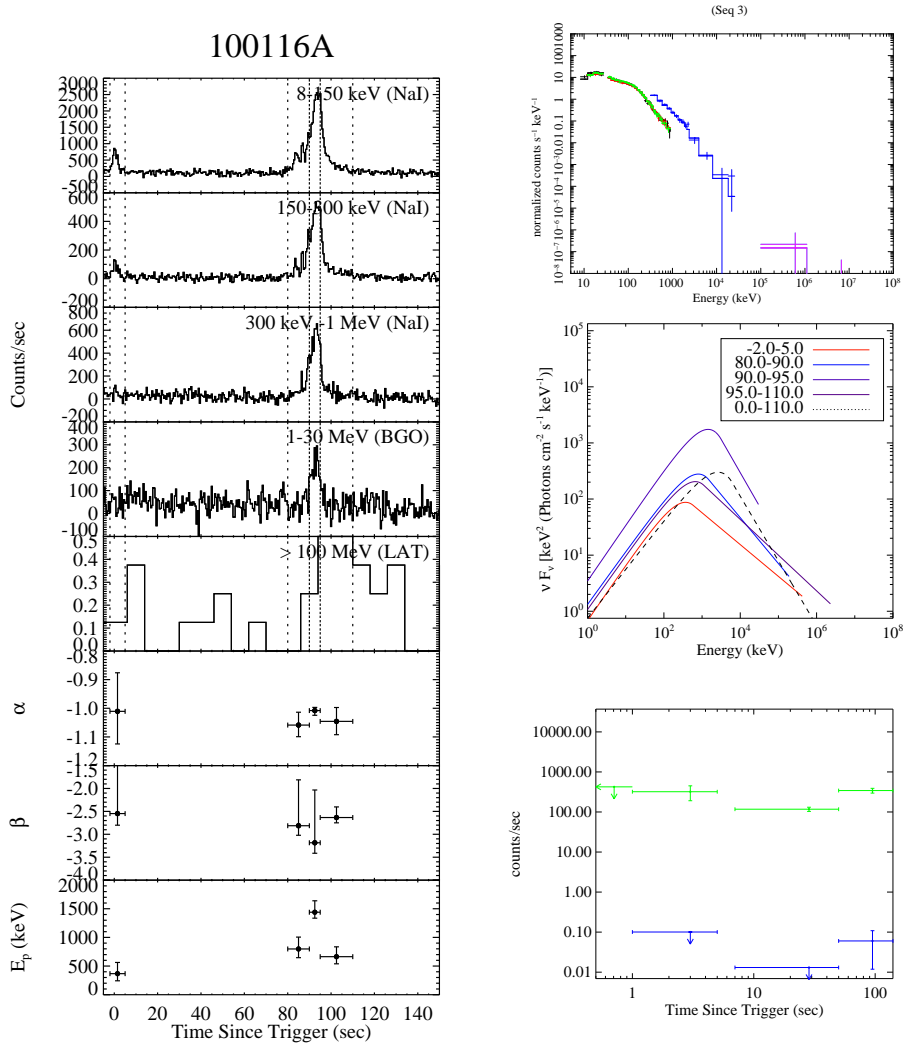


Fig. 14.— Same as Figure 1, but for GRB 100116A.

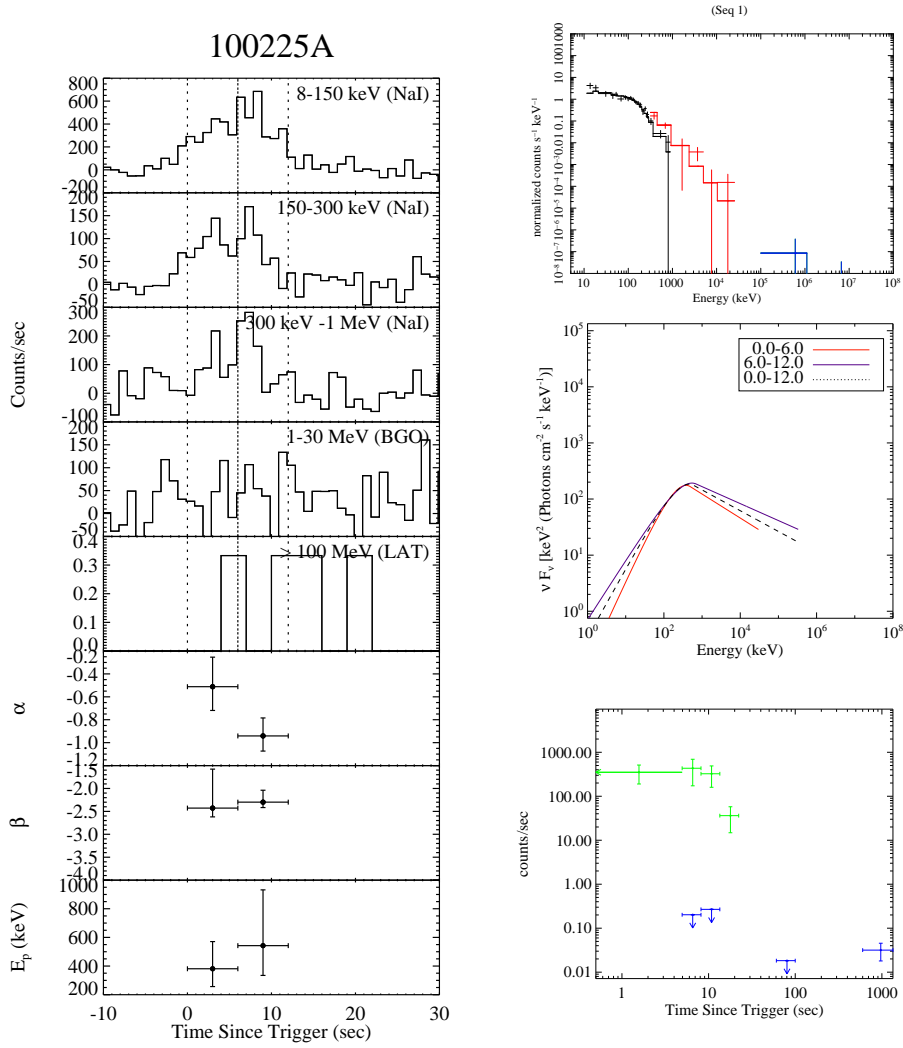


Fig. 15.— Same as Figure 1, but for GRB 100225A.

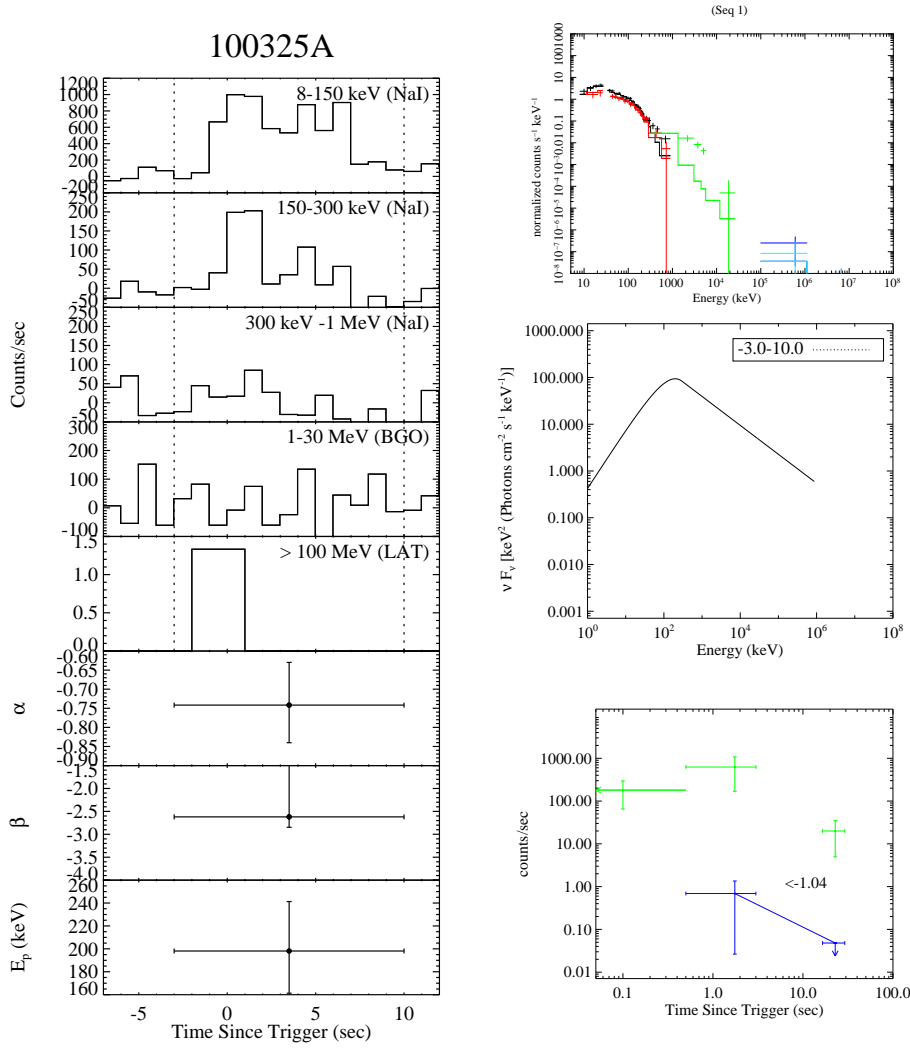


Fig. 16.— Same as Figure 1, but for GRB 100325A.

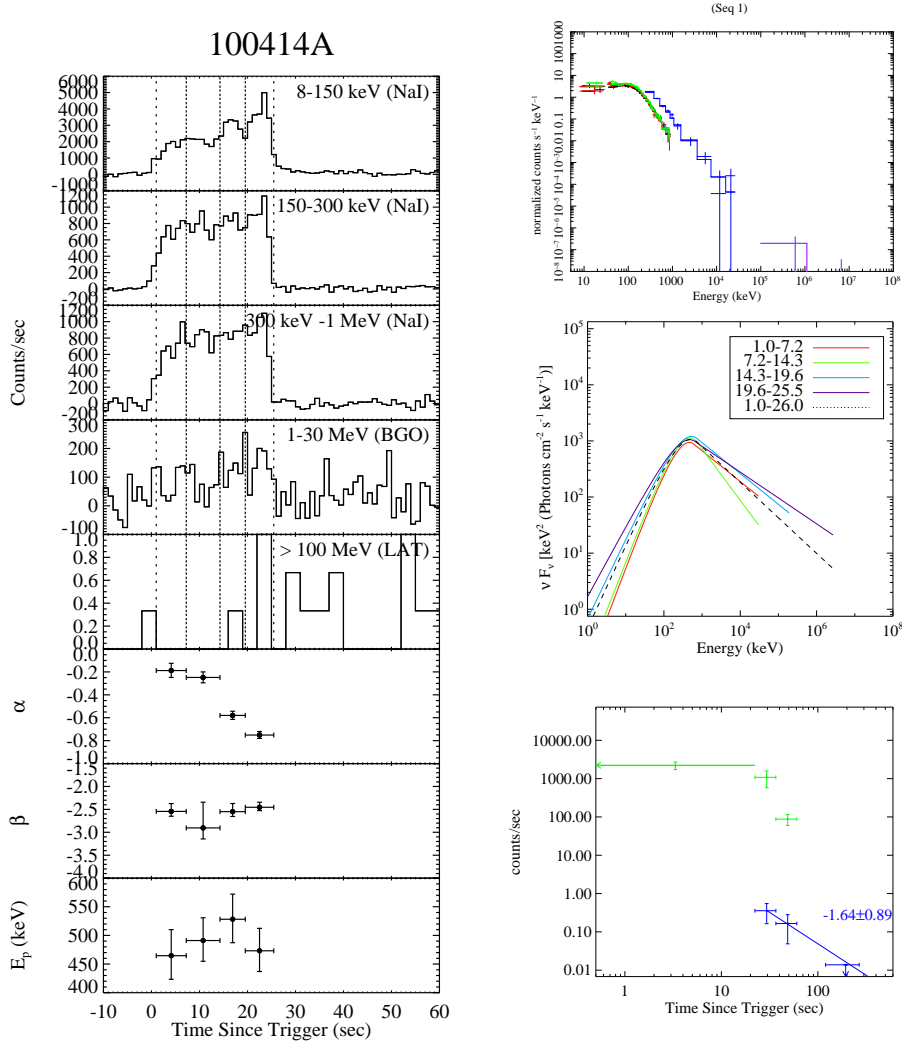


Fig. 17.— Same as Figure 1, but for GRB 100414A.

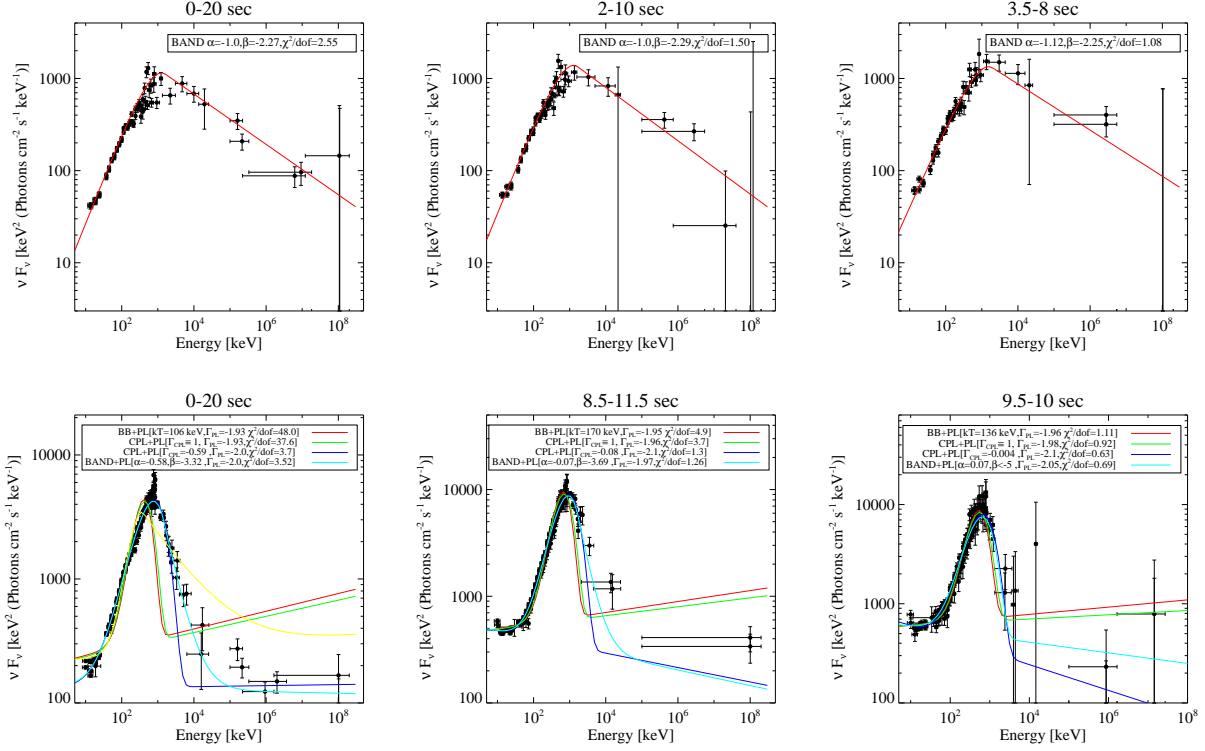


Fig. 18.— A comparison between GRB 080916C and GRB 090902B. *Upper panel:* The case of GRB 080916C. The Band parameters are $(\alpha, \beta) = (-1.0, -2.27), (-1.0, -2.29), (-1.12, -2.25)$ for 0-20 s, 2-10 s, and 3.5-8 s, respectively. Little spectral parameter variation is seen with reducing time bins. *Lower panel:* The case of GRB 090902B. (1) For 0-20 s, the Band+PL model ($\alpha = -0.58, \beta = -3.32, \Gamma_{\text{PL}} = -2.0$ with $\chi^2/\text{dof} = 3.52$) and the CPL+PL model ($\Gamma_{\text{CPL}} = -0.59, \Gamma_{\text{PL}} = -2.0$ with $\chi^2/\text{dof} = 3.7$) give marginally acceptable fits to the data. The CPL+PL model with $\Gamma_{\text{CPL}} = 1$ (Rayleigh-Jeans) and the BB+PL model give unacceptable fits. (2) For 8.5-11.5 s, the Band+PL model ($\alpha = -0.07, \beta = -3.69, \Gamma_{\text{PL}} = -1.97$ with $\chi^2/\text{dof} = 1.26$) and the CPL+PL model ($\Gamma_{\text{CPL}} = -0.08, \Gamma_{\text{PL}} = -2.1$ with $\chi^2/\text{dof} = 1.3$) give acceptable fits to the data. The CPL+PL model with $\Gamma_{\text{CPL}} = 1$ ($\chi^2/\text{dof} = 3.7$) and the BB+PL model ($\chi^2/\text{dof} = 4.9$) give marginally acceptable fits. (3) 9.5-10 s, the Band+PL model ($\alpha = 0.07, \beta < -5, \Gamma_{\text{PL}} = -2.05$ with $\chi^2/\text{dof} = 0.69$) can only give an upper limit on β . The CPL+PL model ($\Gamma_{\text{CPL}} = -0.0004, \Gamma_{\text{PL}} = -2.1$ with $\chi^2/\text{dof} = 0.63$) give marginally acceptable fit to the data. On the other hand, the CPL+PL model with $\Gamma_{\text{CPL}} = 1$ ($\chi^2/\text{dof} = 0.92$) and the BB+PL model ($\chi^2/\text{dof} = 1.11$) give acceptable fits. Clear narrowing trend is seen when the time bins get smaller.

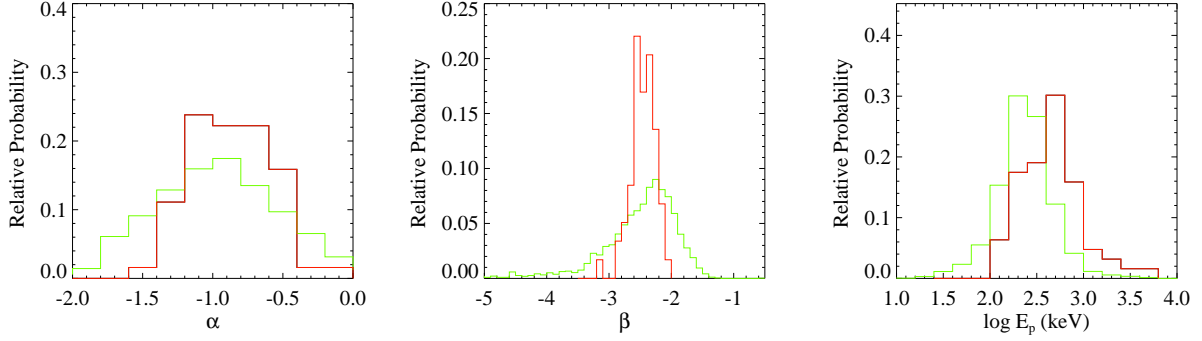


Fig. 19.— Distributions of the Band-function parameters α , β , and E_p in our sample (red) in comparison with the BATSE bright sources sample (green). The BATSE sample is adopted from Preece et al. (2000).

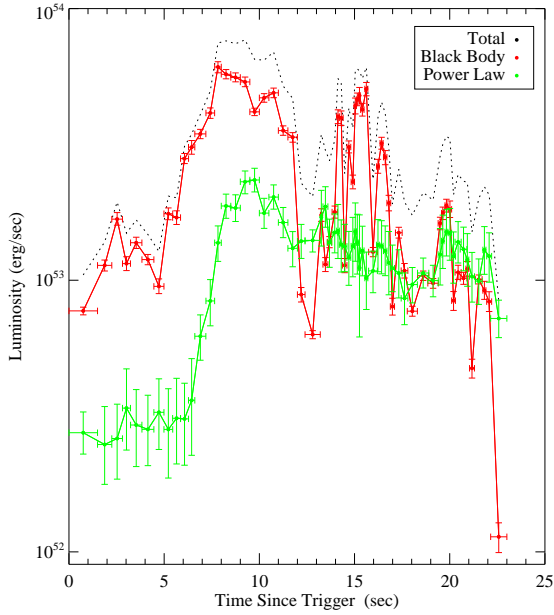


Fig. 20.— A comparison between the lightcurves of the blackbody component (red) and the power-law component (green) in GRB 090902B. The total lightcurve (the sum of the two components, *dotted* line) is also shown for comparison.

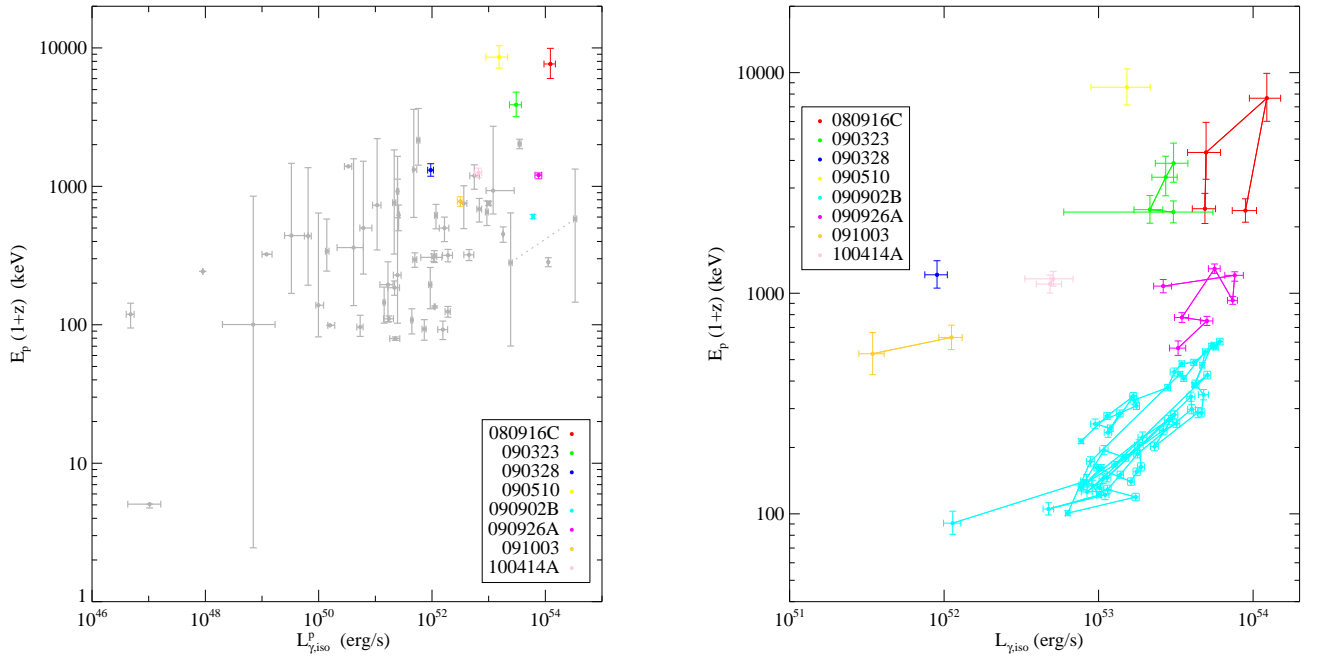


Fig. 21.— The global $L_{\gamma,iso}^p$ vs. $E_p(1+z)$ correlation (panel a) and internal $L_{\gamma,iso}$ vs. $E_p(1+z)$ correlation (panel b) for the 8 *Fermi*/LAT GRBs with known redshifts. The grey dots in (a) are previous bursts taken from Zhang et al. (2009).

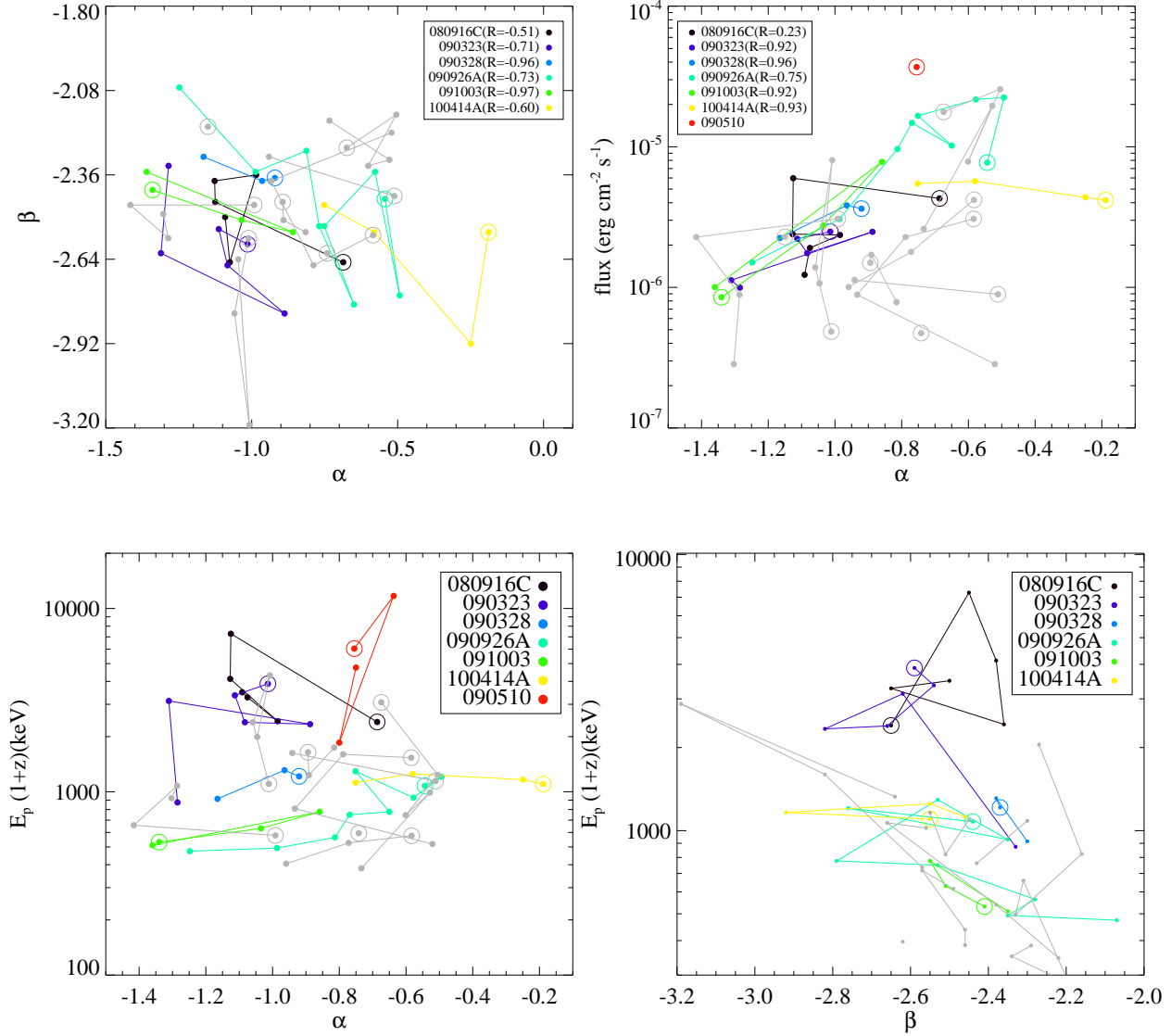


Fig. 22.— The two dimension plots of various pairs of spectral parameters. (a) $\alpha - \beta$, with linear Pearson correlation coefficients for individual bursts marked in the inset; (b) α -flux, with linear Pearson correlation coefficients for individual bursts marked in the inset; (c) $E_p - \alpha$; (d) $E_p - \beta$. For those burst without redshift, $z = 2.0$ is assumed (grey symbols and lines).

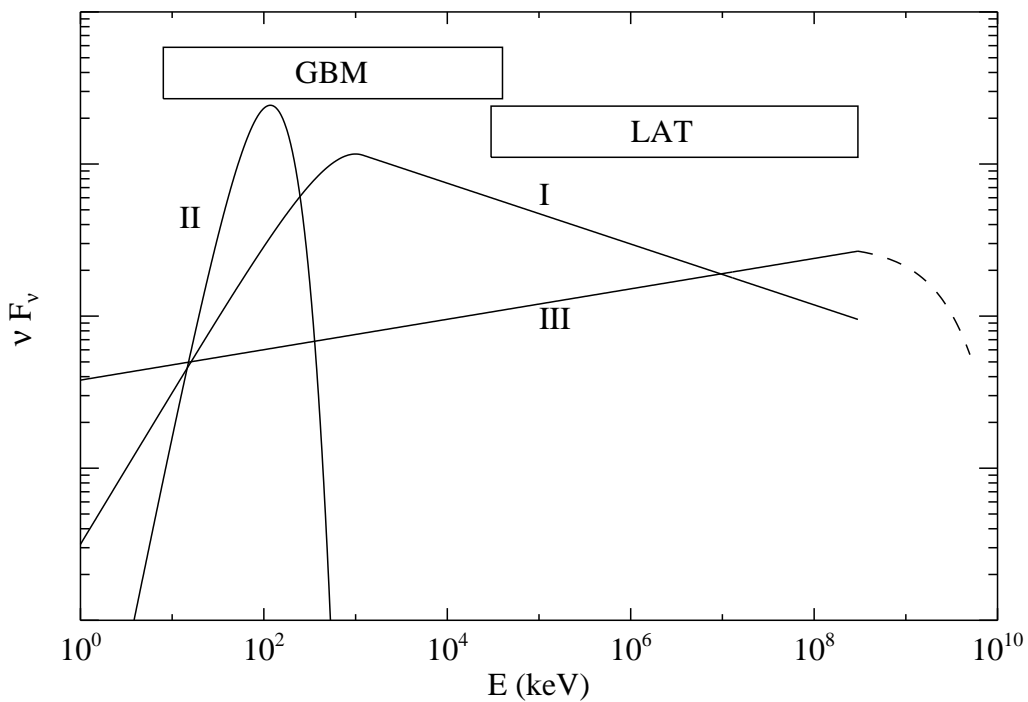


Fig. 23.— A cartoon picture of three elemental spectral components that shape GRB prompt emission spectra: (I) a Band-function component that is likely of the non-thermal origin; (II) a quasi-thermal component; and (III) an extra power-law component that extends to high energy, which is expected to have a cut-off near or above the high energy end of the LAT energy band.

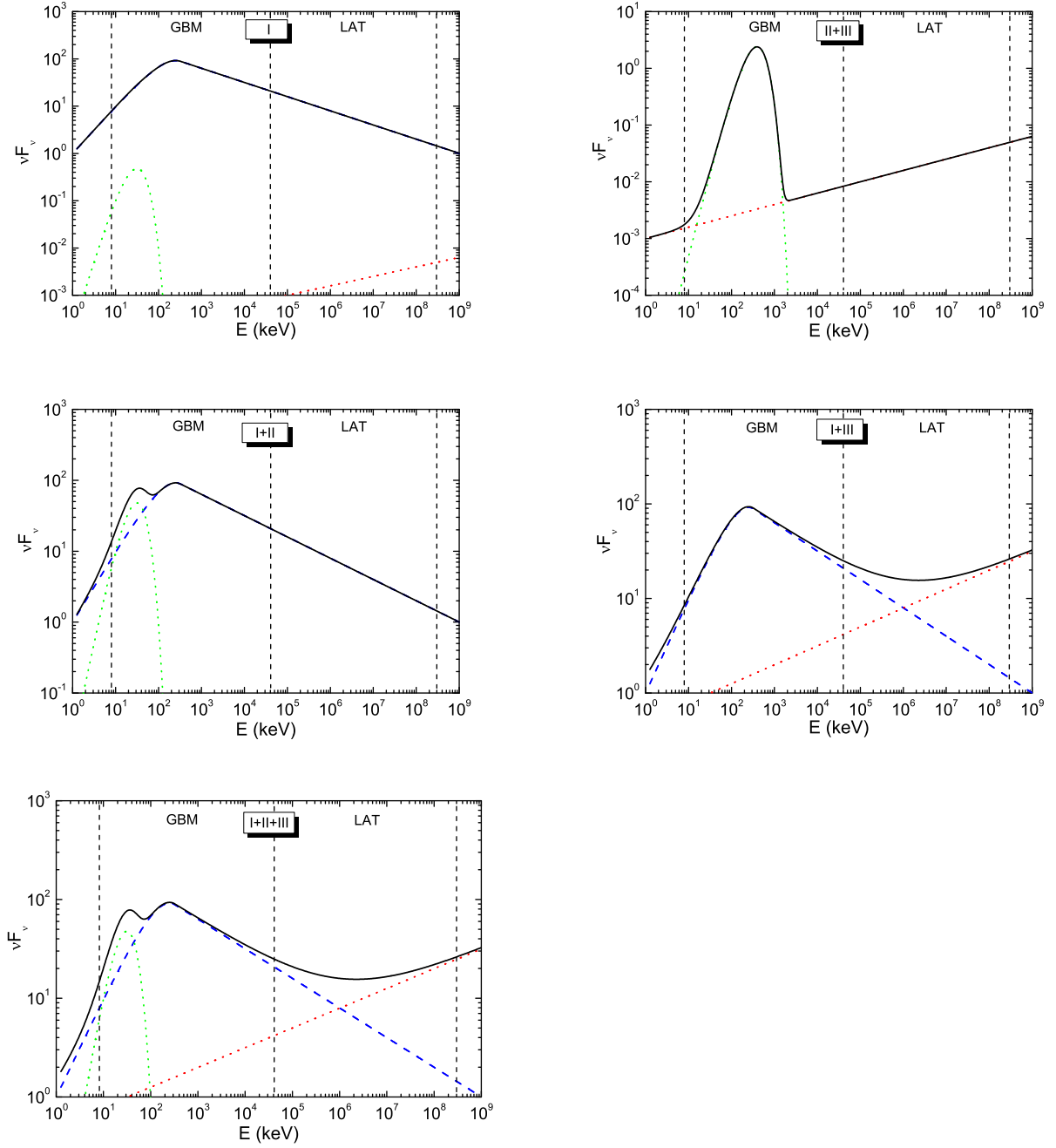


Fig. 24.— Five possible spectral combinations with the three spectral components.

